The Planetary Science Journal 5:182 24pp), 2024 August https: doi.org 10.3847 PSJ ad62f5

The Dynamical State of the Didymos System before and after the DART Impact

Derek C. Richardson[1], Harrison F. Agrusa[1,2], Brent Barbee[3], Rachel H. Cueva[4], Fabio Ferrari[5], Seth A. Jacobson[6], Rahil Makadia[7], Alex J. Meyer[4], Patrick Michel[2,8], Ryota Nakano[9,10], Yun Zhang[11], Paul Abell[12], Colby C. Merrill[13], Adriano Campo Bagatin[14], Olivier Barnouin[15], Nancy L. Chabot[15], Andrew F. Cheng[15], Steven R. Chesley[16], R. Terik Daly[15], Siegfried Eggl[17,18], Carolyn M. Ernst[15], Eugene G. Fahnestock[16], Tony L. Farnham[1], Oscar Fuentes-Muñoz[4], Edoardo Gramigna[19], Douglas P. Hamilton[1], Masatoshi Hirabayashi[9,20], Martin Jutzi[21], Josh Lyzhoft[3], Riccardo Lasagni Manghi[19], Jay McMahon[4], Fernando Moreno[22], Naomi Murdoch[23], Shantanu P. Naidu[16], Eric E. Palmer[24], Paolo Panicucci[5], Laurent Pou[16], Petr Pravec[25], Sabina D. Raducan[21], Andrew S. Rivkin[15], Alessandro Rossi[26], Paul Sánchez[27], Daniel J. Scheeres[4], Peter Scheirich[25], Stephen R. Schwartz[14,24], Damya Souami[2,28,29,30], Gonzalo Tancredi[31], Paolo Tanga[2], Paolo Tortora[19,32], Josep M. Trigo-Rodríguez[33], Kleomenis Tsiganis[34], John Wimarsson[21], and Marco Zannoni[19,32]

[1] Department of Astronomy, University of Maryland, College Park, MD 20742, USA; dcr@umd.edu
[2] Université Côte d Azur, Observatoire de la Côte d Azur, CNRS, Laboratoire Lagrange Bd de l Observatoire, CS 34229 06304 Nice Cedex 4, France
[3] NASA Goddard Space Flight Center, Greenbelt, MD 20771, USA
[4] Smead Department of Aerospace Engineering Sciences, University of Colorado Boulder, 3775 Discovery Drive, Boulder, CO 80303, USA
[5] Department of Aerospace Science and Technology, Politecnico di Milano, Milan 20159, Italy
[6] Department of Earth and Environmental Sciences, Michigan State University, East Lansing, MI 48824, USA
[7] Department of Aerospace Engineering, University of Illinois at Urbana-Champaign, Urbana, IL 61801, USA
[8] The University of Tokyo, Department of Systems Innovation, School of Engineering, Hongo 7-3-1, Bunkyo-ku, Tokyo 113-0033, Japan
[9] Daniel Guggenheim School of Aerospace Engineering, Georgia Institute of Technology, Atlanta, GA 30332, USA
[10] Department of Aerospace Engineering, Auburn University, Auburn, AL 36849, USA
[11] Department of Climate and Space Sciences and Engineering, University of Michigan, Ann Arbor, MI 48109, USA
[12] Johnson Space Center, Houston, TX 77058, USA
[13] Sibley School of Mechanical and Aerospace Engineering, Cornell University, Ithaca, NY 14853, USA
[14] Instituto de Fisica Aplicada a las Ciencias y las Tecnologias IUFACyT), Universidad de Alicante, Ctra. Sant Vicent del Raspeig s n, 03690, Sant Vicent del Raspeig, Alicante, Spain
[15] Johns Hopkins University Applied Physics Laboratory, Laurel, MD 20723, USA
[16] Jet Propulsion Laboratory, California Institute of Technology, Pasadena, CA 91109, USA
[17] Department of Aerospace Engineering Astronomy, University of Illinois at Urbana-Champaign, Urbana, IL 61801, USA
[18] National Center for Supercomputing Applications, University of Illinois at Urbana-Champaign, Urbana, IL 61801, USA
[19] Department of Industrial Engineering, Alma Mater Studiorum—Università di Bologna, Forlì FC) 47121, Italy
[20] Department of Geosciences, Auburn University, Auburn, AL 36849, USA
[21] Space Research and Planetary Sciences, Physics Institute University of Bern, Bern 3012, Switzerland
[22] Instituto de Astro sica de Andalucia, CSIC, 18008 Granada, Spain
[23] Institut Supérieur de l Aéronautique et de l Espace ISAE-SUPAERO), Université de Toulouse, Toulouse, France
[24] Planetary Science Institute, Tucson, AZ 85719, USA
[25] Astronomical Institute of the Academy of Sciences of the Czech Republic, Fri ova 298 Ondrejov, CZ 25165, Czech Republic
[26] Istituto di Fisica Applicata "Nello Carrara" IFAC-CNR), Sesto Fiorentino 50019, Italy
[27] Colorado Center for Astrodynamics Research, University of Colorado Boulder, 3775 Discovery Drive, Boulder, CO 80303, USA
[28] LESIA, Observatoire de Paris, Université PSL, CNRS, Sorbonne Université, Université de Paris, 5 place Jules Janssen, F-92195 Meudon, France
[29] Departments of Astronomy, and of Earth and Planetary Science, University of California Berkeley, 501 Campbell Hall, Berkeley, CA 94720-3411, USA
[30] naXys, Department of Mathematics, University of Namur, Rue de Bruxelles 61, 5000 Namur, Belgium
[31] Departamento de Astronomía, Facultad de Ciencias, Udelar, Uruguay
[32] Centro Interdipartimentale di Ricerca Industriale Aerospaziale, Alma Mater Studiorum—Università di Bologna, Forlì FC) 47121, Italy
[33] Institute of Space Sciences CSIC-IEEC), Campus UAB, c Can Magrans s n, Cerdanyola del vallès, Barcelona, Catalonia, Spain
[34] Department of Physics, Aristotle University of Thessaloniki, GR 54124 Thessaloniki, Greece
Received 2023 September 28; revised 2024 June 21; accepted 2024 July 3; published 2024 August 23

Abstract

NASA s Double Asteroid Redirection Test DART) spacecraft impacted Dimorphos, the natural satellite of 65803) Didymos, on 2022 September 26, as a rst successful test of kinetic impactor technology for deflecting a potentially hazardous object in space. The experiment resulted in a small change to the dynamical state of the Didymos system consistent with expectations and Level 1 mission requirements. In the preencounter paper, predictions were put forward regarding the pre- and postimpact dynamical state of the Didymos system. Here we assess these predictions, update preliminary ndings published after the impact, report on new ndings related to dynamics, and provide implications for ESA s Hera mission to Didymos, scheduled for launch in 2024 October with arrival in 2026 December. Preencounter predictions tested to date are largely in line with observations, despite the unexpected, flattened appearance of Didymos compared to the radar model and the apparent preimpact oblate shape of Dimorphos with implications for the origin of the system that remain under investigation). New ndings include that Dimorphos likely became prolate due to the impact and may have entered a tumbling rotation state. A

possible detection of a postimpact transient secular decrease in the binary orbital period suggests possible dynamical coupling with persistent ejecta. Timescales for damping of any tumbling and clearing of any debris are uncertain. The largest uncertainty in the momentum transfer enhancement factor of the DART impact remains the mass of Dimorphos, which will be resolved by the Hera mission.

Uni ed Astronomy Thesaurus concepts: Asteroids 72); Asteroid dynamics 2210); Asteroid satellites 2207)

1 Introduction

On 2022 September 26, NASA s Double Asteroid Redirection Test DART) spacecraft impacted Dimorphos, the natural satellite of 65803) Didymos, as the rst full-scale demonstration of the kinetic impact deflection technique Daly et al. 2023). Prior to intercept, the Didymos system was not a hazard to Earth, and the experiment did not increase the likelihood of collision Makadia et al. 2022). Rather, the impact reduced the orbital period of Dimorphos around Didymos by 33.0 ± 1.0 3) minutes, from 11.92 to 11.37 hr Thomas et al. 2023). Preliminary modeling found this corresponded to an along-track orbital speed change of 2.70 ± 0.10 1) mm s ^{1} for the satellite, implying a momentum transfer enhancement factor ratio of target momentum change to spacecraft momentum, accounting for any ejecta boost) of $\beta = 3.61^{+0.19}_{-0.25}$ 1) assuming a bulk density of 2400 kg m ^{3} Cheng et al. 2023). These results, together with later analyses Chabot et al. 2024), indicate DART met all of its Level 1 requirements, namely to impact Dimorphos, to change the orbital period by at least 73 s, to measure the period change to an accuracy of 7.3 s, and to measure β Rivkin et al. 2021). There was no direct mass measurement of Dimorphos, so β ranges plausibly from 2.2 to 4.9, assuming a Dimorphos bulk density range of 1500–3300 kg m ^{3}. Hera, ESA s follow-on mission to the Didymos system with a planned launch in 2024 October and rendezvous in late 2026 December, promises to constrain the postimpact mass of Dimorphos and therefore β to much higher precision Michel et al. 2022). Together, Hera and DART comprise the Asteroid Impact and Deflection Assessment cooperation between ESA and NASA.

Prior to DART s encounter, Richardson et al. 2022) put forward predictions for the dynamical state of the Didymos system before and after the DART impact based on best-available data and modeling. Table 1 summarizes the main predictions of both the pre- and postimpact dynamical states and their evaluation in light of observations during and after encounter. Table 2 provides an update on key dynamical parameters from the best-available data and analysis, noting that in some cases different approaches give slightly different values, as indicated in the table footnotes see the primary sources for more details).

In the remainder of this paper, we expand on the postencounter observations and dynamics implications in detail. Section 2 describes constraints on the perturbed dynamics of the system from observations of the postimpact mutual binary orbit, with implications for the possible new shape and spin state of the secondary, limits on the system mass distribution, and the possible importance of postimpact ejecta momentum exchange. Section 3 provides an update on the β estimate, including progress toward measuring the heliocentric momentum change, modeling of exchanges between ejecta fragments and the binary components, and the effect of surface curvature on recoil ef ciency. Section 4 provides implications for the inferred component rubble structure in light of new observations, the possible origin of the oblate preimpact shape of Dimorphos, effects on β and the rotation state arising from possible reshaping of the secondary, and implications for secular effects driven by tides and BYORP over year-long timescales. Section 5 presents expectations for Hera given our best assessment of the postimpact dynamical state of the system. Section 6 summarizes our conclusions from this work. The reader is referred to companion papers in this focus issue to form a complete picture of the aftermath of the DART mission.

2 Perturbed Dynamics

Spin–orbit coupling is common in binary asteroids due to their generally irregular shapes and close mutual proximity. Thus, binary asteroids are best modeled by the full two-body problem F2BP). We can numerically simulate the dynamics of binary asteroids by integrating the F2BP using software such as the General Use Binary Asteroid Simulator GUBAS; Davis & Scheeres 2020, 2021). The effects of perturbations are also strongly coupled as explored in detail in Meyer et al. 2023b). The observed changes in the orbit of Dimorphos allow us to constrain the properties of the system in the following way. The impact decreased the semimajor axis of the system and increased its eccentricity at least initially; see Section 2.4). As a result, the system was perturbed out of equilibrium and the argument of periapsis precessed at the rate given in Table 2. Simultaneously, the rotation state of Dimorphos was probably excited in the impact Section 2.2), and its evolution was coupled to the evolution of the binary eccentricity and semimajor axis. The tangential component of the orbital-velocity change V_T) is one of the main measurements that allows us to bridge preencounter and postencounter states, giving insight into the dynamical parameters.

Based on the initial results published by Li et al. 2023), Thomas et al. 2023), and Cheng et al. 2023), Daly et al. 2023) calculated $V_T = 2.7 \pm 0.1$ mm s ^{1} due to the DART impact. This calculation was corroborated by Meyer et al. 2023b), who go on to calculate the change in eccentricity and semimajor axis of the orbit. Using so-called "observable elements," de ned using only the physical separation between the two asteroids, they report a postimpact observable eccentricity of 0.027 ± 0.001 and a postimpact observable semimajor axis of 1189 ± 17 m.

Since these publications, the postimpact measurements of the system have been re ned. Using the iterative algorithm de ned in Agrusa et al. 2021) and Meyer et al. 2023b), the nominal parameters of the pre- and postimpact Didymos–Dimorphos system listed in Table 2) lead to an estimate of the system s bulk density equal to 2.79 g cm ^{3}. This value of the bulk density is in line with the bulk densities measured for other S-type asteroids: somewhat higher than Itokawa 1.95 g cm ^{3}), but similar to Eros and Ida 2.6 g cm ^{3}; Belton et al. 1995; Wilkison et al. 2002; Abe et al. 2006). This is also between the density of 66391) Moshup 1.97 g cm ^{3}) and its secondary Squannit 2.81 g cm ^{3}; Ostro et al. 2006).

Table 1
Summary of Preencounter Predictions and their Postencounter Evaluation

Prediction	Evaluation
The system at encounter will be in a low-energy state, with small zero eccentricity, no excited modes, and Dimorphos tidally locked to Didymos; no recent big impacts or encounters.	Insuf cient observational constraints of the preimpact state at encounter; low zero eccentricity consistent with modeled low postimpact eccentricity Section 2); Dimorphos s apparent preimpact oblate shape consistent with undetectable signature of rotation in lightcurves, implying slow but not necessarily zero tidal damping Section 4); no indication of excitement from recent perturbation but not ruled out.
Impact yields β between 1 and 5, reducing orbital period for $\beta > 1$) and inducing few minute orbital-period variations; heliocentric β may be measurable.	β between 2.2 and 4.9 for plausible Dimorphos bulk density; period reduced by $\sim$ 33 min but postimpact nonsecular variations unobservable due to high frequency Section 2); successful future heliocentric β measurement likely Section 3).
Impact alters rotation state, inducing libration; may excite instability depending on Dimorphos s inertia moments.	Postimpact secondary lightcurve minima offsets from mutual events consistent with libration of a few tens of degrees amplitude Section 2); observed varying postimpact secondary lightcurve amplitude and postimpact orbit modeling consistent with possible non-principal-axis NPA) rotation state tumbling Section 4).
Shape change of either body could change β measurably.	No Didymos spin change detected to 1 s precision Section 4); Dimorphos likely reshaped due to detection of secondary lightcurve Section 4).
Postimpact secular effects tidal friction, binary Yarkovsky–O'Keefe–Radzievskii–Paddack BYORP)) may alter system state prior to Hera arrival.	Possible postimpact drop s) in eccentricity and orbital period Section 2) noted in postimpact orbit modeling but likely too soon as of this writing to observe measurable effects of tides BYORP Section 4).

Table 2
Selected Dynamical Parameters of the Didymos System before and after the DART Impact[a]

Parameter	Preencounter	Preimpact	Postimpact
Volume-equivalent Diameter of Primary[b] m]	780 ± 30	730 ± 17	assumed unchanged
Volume-equivalent Diameter of Secondary[c] m]	164 ± 18	150.0 ± 2.5	assumed unchanged
Bulk Density of Primary, Secondary[d] kg m ^{3}]	2170 ± 350 both)	2790 ± 140, 2400 ± 300	assumed unchanged
Mean Separation of Component Centers[e] km]	1.20 ± 0.03	1.189 ± 0.017	1.152 ± 0.018
Secondary Shape[f] a_s b_s, b_s c_s	1.3 ± 0.2, 1.2	1.06 ± 0.03, 1.47 ± 0.04	1.300 ± 0.010, 1.3 ± 0.2
Total Mass of System[g] 10^{11} kg]	5.55 ± 0.42	5.3 ± 0.2	assumed unchanged
Mutual Orbital Period[h] hr]	11.921629 ± 0.000003	11.921493 ± 0.000016	11.3674 ± 0.0004
Mutual Orbital Eccentricity[i]	<0.03	<0.03	0.0274 ± 0.0015
Primary Rotation Period[j] hr]	2.2600 ± 0.0001	2.2600 ± 0.0001	2.260 ± 0.001
Secondary Rotation Period[k] hr]	11.921629 ± 0.000003	11.92149 ± 0.00002	pending
Secondary Orbital Inclination]	0 assumed)	0 assumed)	pending
Apsidal Precession Rate[l] day ^{1}]			6.7 ± 0.2

Notes
[a] "Preencounter" values are from Richardson et al. 2022) before DART s arrival in the system. "Preimpact" using DART data) and "Postimpact" values are from just prior to and just after the DART impact, respectively, based on the latest measurements and modeling as of this writing. Uncertainties are 1 .
[b] Preimpact value from Barnouin et al. 2024).
[c] Preimpact value from Daly et al. 2024).
[d] Preimpact values from Naidu et al. 2024) for Didymos and Daly et al. 2023) for Dimorphos. A larger preencounter bulk density estimate of 2370 ± 300 kg m ^{3} for both is reported by Scheirich & Pravec 2022).
[e] Preimpact value from Naidu et al. 2024); postimpact change in value from Meyer et al. 2023a).
[f] Preimpact values from Daly et al. 2024); postimpact values from Naidu et al. 2024). Note: the shape of Dimorphos is not directly measured postimpact in this model. The reported axis ratios correspond to the shape of an ellipsoid having the same moments of inertia. Pravec et al. 2024) nd a postimpact range of 1.1–1.4 for a_s b_s.
[g] Preimpact value from Naidu et al. 2024).
[h] Pre- and postimpact values from Naidu et al. 2024). Using a different model, Scheirich et al. 2024) nd a postimpact value of 11.3675 ± 0.0004 hr.
[i] Preimpact value from Scheirich & Pravec 2009); postimpact value from Naidu et al. 2024). Scheirich et al. 2024) nd a postimpact value of 0.028 ± 0.005, but possibly dropping to zero 70 days after impact gives the best t in their model see Section 2.4).
[j] Preimpact value from Pravec et al. 2006); postimpact value from J. Ďurech & P. Pravec 2024, in preparation).
[k] Preimpact value assumed to be same as secondary orbital period tidal lock).
[l] Value from Naidu et al. 2024). Scheirich et al. 2024) nd $7.^{\circ}3 \pm 0.^{\circ}7$ day ^{1} in their model.

Using the calculated change in semimajor axis from Meyer et al. 2023b), we nd a postimpact observable semimajor axis of 1152 ± 18 m. The measured postimpact eccentricity is consistent with a physically circular preimpact orbit, as described in Meyer et al. 2023b).

Similar to the approach in Meyer et al. 2023a), we iterate the system mass to match the preimpact orbital period, then iterate the tangential V_T until we match the postimpact orbital period. Using this approach with the updated nominal postimpact system, we calculate a nominal V_T of 2.42 mm s ^{1}. Interestingly, Naidu et al. 2024) calculate a V_T of 2.62 mm s ^{1}, slightly larger than our value. Our smaller value is the result of the change in orbital period caused by secondary reshaping Nakano et al. 2022; Meyer et al. 2023b). However, these values are largely consistent when considering the system uncertainties.

2.1. Orbital Precession

The measured postimpact precession rate of around $6\overset{\circ}{.}7$ day^{-1} warrants discussion Naidu et al. 2024; Scheirich et al. 2024). The J_2 value reported in Naidu et al. 2024), estimated using an orbit t matching the photometry data, is about 0.092. For a detailed discussion of the methods used for this estimation, see Naidu et al. 2022) This is consistent with a uniform-density distribution in Didymos and suggests a much faster precession rate, around 13° day ^{1} using classical perturbation theory Murray & Dermott 2000). One interpretation of this discrepancy is that Didymos in reality has an overdense interior that decreases its effective J_2. However, a reduction in J_2 of around 50 that is required to achieve the observed precession rate is physically unrealistic, requiring an inner core with a radius equal to the polar radius of Didymos and a density of 4–5 g cm ^{3}, which is unrealistic for a rubble-pile S-type asteroid such as Didymos.

Another consideration is how the secondary s elongation and libration affect the system s precession rate, as shown by Ćuk & Nesvorný 2010). Meyer et al. 2021) demonstrated that both the β value of the impact and the secondary s elongation affect the apsidal precession of the orbit. Once Cheng et al. 2023) estimated the impact s β, Meyer et al. 2023b) calculated that increasing the postimpact elongation of Dimorphos reduced the system s precession rate. We note the apsidal precession rate is given by the expression Ćuk & Nesvorný 2010)

$$\dot{\varpi} = \frac{3}{2}\frac{J_2 n}{a^2(1-e^2)^2} + \frac{C_{22}a\sqrt{1-e^2}}{e} \times \left[9\cos 2\phi \cos f + 6\sin 2\phi \sin f \frac{2+e\cos f}{1+e\sin f}\right], \quad (1)$$

where f is the true anomaly, is the secondary s physical libration angle, a is the semimajor axis, e is the eccentricity, n is the mean motion, and J_2 and C_{22} are the second-degree gravity terms. Changing the elongation of the secondary changes its C_{22} gravity term, which affects the precession rate. We also note how both the libration angle and true anomaly appear in this expression. By changing the β value of the impact, the relationship between these two angles will also change, again affecting the precession rate. Furthermore, larger impact β values also result in a smaller semimajor axis and larger eccentricity. This demonstrates the complex nature of orbital precession in perturbed binary asteroid systems.

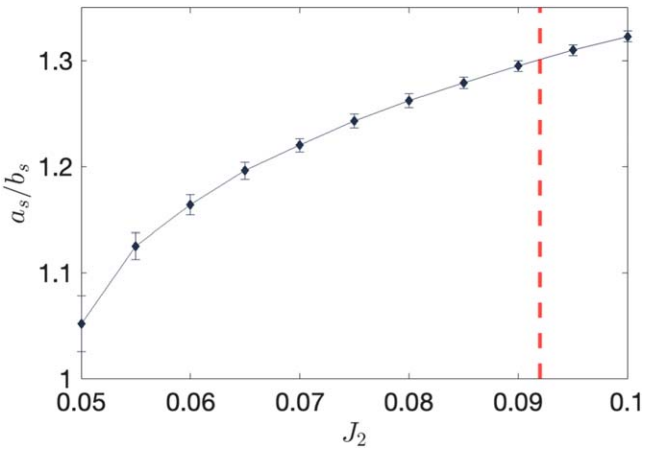

Figure 1 For the observed precession rate of the mutual orbit, the curve indicates the necessary Dimorphos elongation for a given J_2 value for Didymos, with error bars corresponding to the uncertainty on the precession rate measurement. The homogeneous density J_2 is shown as a red dashed line, which corresponds to a uniform-density distribution in Didymos.

Thus, we nd a degeneracy in explaining the orbital precession rate, as both the primary s interior structure and the elongation and libration of Dimorphos can contribute to the observed value. To illustrate, using fully coupled numerical simulations we plot the necessary Dimorphos elongation, a_s b_s, as a function of the primary s J_2, in Figure 1. This curve represents possible combinations of primary oblateness and secondary elongation that can account for the observed precession rate. When accounting for the secondary s libration, the estimate in Naidu et al. 2024) suggests a J_2 value largely consistent with a homogeneous density distribution in Didymos, shown as a dashed red line in Figure 1.

Furthermore, lightcurves suggest a more elongated secondary with a_s b_s between 1.1 and 1.4 Pravec et al. 2024), also indicating a homogeneous density distribution within Didymos. To go along with their estimate of J_2, Naidu et al. 2024) also estimate an elongated secondary around a_s $b_s = 1.3$. These results are consistent with impact simulations suggesting a global reshaping of Dimorphos Raducan et al. 2024a). The reshaping of Dimorphos could also substantially affect its postimpact orbital-period change and rotational state see Section 4.4 for details).

2.2. Dimorphos s Rotation

The rotation state of Dimorphos is of particular interest to Hera Section 5), which will deploy two CubeSats to perform proximity operations around the secondary. The likely circular preimpact orbit indicates a lack of substantial forced libration in Dimorphos prior to the impact, meaning the secondary s rotation rate is nearly identical to the orbit rate over the full orbit. Thus, the typical assumption of a perfectly synchronous preimpact secondary still holds Richardson et al. 2022). We can therefore determine the minimum amount of libration in the postimpact system, which occurs if DART impacted in line with the center of mass of Dimorphos.

To investigate the postimpact rotation of Dimorphos, we perform high- delity numerical simulations using GUBAS, Davis & Scheeres 2021) following the methodology from Agrusa et al. 2021): we apply a V_T to Dimorphos when it is rotating synchronously with the preimpact orbital period, then simply track the postimpact attitude of the perturbed secondary

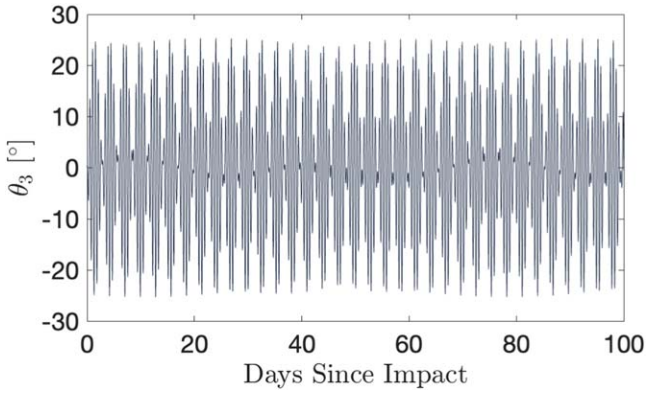

Figure 2 Libration angle of Dimorphos for the nominal system if the impact vector passed through its center of mass.

over time. We use the nominal system parameters Table 2) without uncertainties as inputs for a GUBAS simulation, and integrate for 100 days. This simulation is used to predict the libration amplitude in the system, which has not previously been studied in high- delity simulations. Figure 2 shows the libration angle, measuring the angle between the secondary s long axis and the line connecting the centers of the two bodies, over time for the case where the impact vector passes through the secondary s center of mass, meaning there is no torque imparted by the impact. Thus, this is the minimum amount of libration present in the system, corresponding to an amplitude of $\pm 25°$. We note that this nominal system remains attitude stable after the impact, where rotation only occurs about the secondary s major principal inertial axis. There are several underlying periods driving the behavior of the libration angle, all with periods on the order of hours. Using a fast Fourier transform decomposition, we nd the main frequency of libration has a period around 14 hr, with a secondary period around 11.4 hr equal to the mean motion), and several other minor frequencies. These commensurate periods result in beating in the libration angle.

However, in reality there is still considerable uncertainty surrounding the postimpact secondary shape. As a result, not only are larger libration amplitudes possible, Dimorphos may be in an NPA rotation state i.e., tumbling).[35] The nominal secondary shape given in Table 2, $a_s\ b_s = 1.3\ b_s\ c_s = 1.3$, is near a large region of attitude instability Agrusa et al. 2021). Adjusting the shape slightly can induce attitude instabilities. For example, the 1–2–3 roll, pitch, and yaw Euler angles, measuring the secondary s attitude relative to a rotating Hill frame, for the shape $a_s\ b_s = 1.2$ and $b_s\ c_s = 1.4$, are plotted in Figure 3 for methods, see Agrusa et al. 2021). This demonstrates that not only are larger libration amplitudes possible, the secondary can begin tumbling after the impact. However, this tumbling state of Dimorphos is still on-average synchronous with the orbit rate, so its long axis is still generally pointed toward Didymos. In Figure 3, this is illustrated by the yaw angle θ_3 remaining $<90°$.

The impact and corresponding ejecta almost certainly imparted some amount of torque to Dimorphos, so we now relax our torque-less impact assumption and include a perturbation to the secondary s spin rate. The spin angular

[35] Pravec et al. 2024) indicate that postimpact tumbling is expected for the range of shapes that t their models while Naidu et al. 2024) nd a nontumbling spin state is consistent with their data and cannot be ruled out.

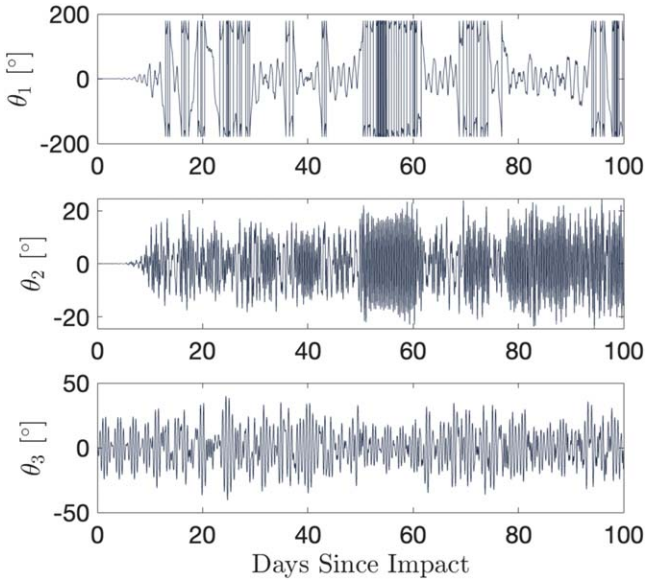

Figure 3 1–2–3 roll, pitch, and yaw Euler angles for the secondary for the tumbling case. On average, the secondary is still tidally locked with the primary.

momentum imparted to Dimorphos is

$$\Delta \boldsymbol{L} = \boldsymbol{r}_{\rm imp} \times \Delta \boldsymbol{p}, \tag{2}$$

where $\boldsymbol{r}_{\rm imp}$ is the impact location of DART relative to the center of mass of Dimorphos and $\Delta \boldsymbol{p}$ is the momentum transfer caused by DART. The spacecraft impacted roughly 25 m off from the center of gure under our uniform-density assumption this is also the center of mass; Daly et al. 2023). The change to Dimorphos s spin vector is then

$$\Delta \boldsymbol{\omega} = \mathbf{I}^{-1}(\boldsymbol{r}_{\rm imp} \times \Delta \boldsymbol{p}), \tag{3}$$

where $\mathbf{I}$ is the unmeasured) inertia tensor of Dimorphos.

The true impact geometry, taken from Daly et al. 2023), does not pass through Dimorphos s center of mass. Importantly, the resultant torque of the impact and ejecta acts to increase the secondary s spin period. On the other hand, the postimpact orbital period is reduced. This means the new Didymos system has a larger difference between the secondary s rotation period and the orbital period than if the impact did not change the spin period, leading to a larger libration amplitude.

The importance of including the impact torque is illustrated in Figure 4. One case includes the effects of the impact s imparted $\boldsymbol{V}$, whereas the other includes both $\boldsymbol{V}$ and . We see larger libration amplitudes when we include the change in rotation rate caused by the impact torque. This demonstrates the importance of the torque imparted by the impact, and shows the predictions by Agrusa et al. 2021) are underestimates.

In a formal analysis of the post-DART rotation state of Dimorphos, Pravec et al. 2024) leverage synthetic lightcurves of Dimorphos to assess the rotational stability of Dimorphos. They nd signi cant NPA rotation is required to reproduce observations of the secondary lightcurves.

2.3. Orbital Period

While the average orbital period has been measured to high accuracy, the instantaneous orbital period will experience

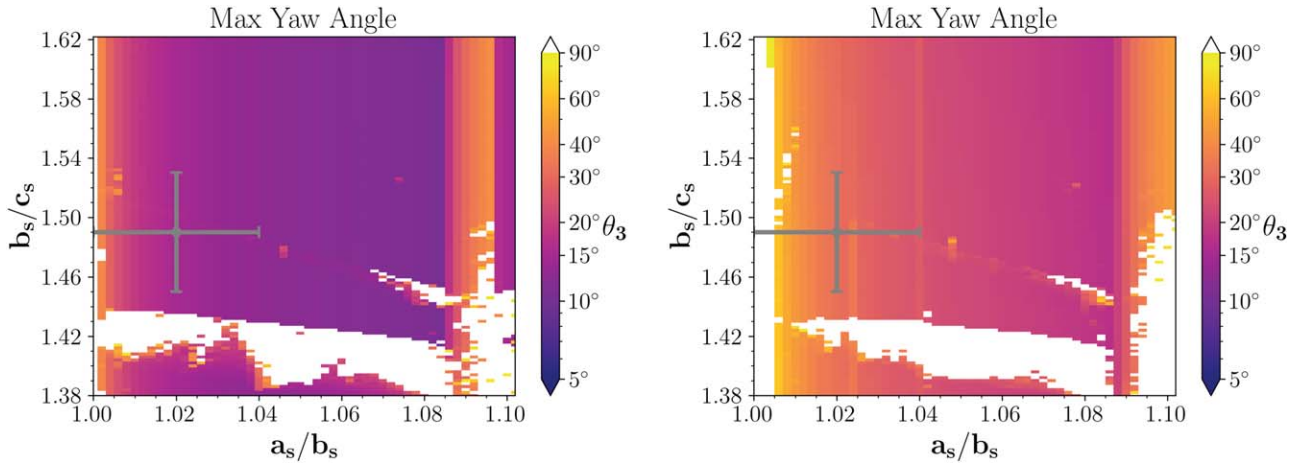

(a) Only including $\Delta\vec{V}$ (b) Including both $\Delta\vec{V}$ and $\Delta\vec{\omega}$

Figure 4 Maximum yaw angle of Dimorphos, comparing the effects of including the impact torque. When this torque is included, the libration amplitude of the postimpact system generally increases on the order of 10°. When is included and Dimorphos has a dynamically equivalent a_s b_s 1.005, the impact can cause Dimorphos to immediately break from synchronous rotation. The shape of the best- t ellipsoid is shown by the gray error bars Daly et al. 2023). The structure of these plots is explained by resonances among Dimorphos s natural frequencies that can trigger attitude instabilities see Agrusa et al. 2021, and references therein).

nonsecular variations due to precession and angular momentum exchange within the system Meyer et al. 2021). In calculating the system s orbital period, it is useful to use the sidereal orbital period, calculated as the time required for the secondary to move 360° around the primary in inertial space Meyer et al. 2021, 2023a). From the simulations we presented above showing the secondary s attitude, we now also plot the sidereal orbital period in Figure 5, for the stable libration system a_s $b_s = 1.3$ and b_s $c_s = 1.1$) and the unstable tumbling system a_s $b_s = 1.2$ and b_s $c_s = 1.4$).

For the stable system, we see two distinct signals in the orbital period. The long-period signal is the result of the orbit s precession, which was measured with observations. The short-period signal is caused by libration within the system, but is likely at too high a frequency and too low an amplitude so that the mean anomaly modulation is less than 1° and is too small to be detected in the data Meyer et al. 2021). This signal could potentially be found by calculating the variation in mutual-event timings over many orbital periods.

In the unstable system, the onset of tumbling removes the periodic behavior from the variations in favor of chaotic behavior. Again, the variations are likely too high in frequency and too low in amplitude for detection, but otherwise they would indicate an unstable rotation state in the secondary. Also note the long-period signal is lost, suggesting that the loss of the precession signal in the observations also indicates tumbling in the secondary. This is consistent with a relatively large reduction in the orbit s eccentricity caused by the onset of secondary tumbling Meyer et al. 2023a).

The detection of these orbital-period variations would require high-quality data over an extended period of time. This is only possible using space-based measurements. Ground-based measurements are limited to sparse coverage and typically combine several nights worth of data Thomas et al. 2023). This approach would average out any small modulations of the orbital period. However, space-based measurements could provide full coverage of several orbital periods. Thus, these measurements may be possible from the Hera spacecraft. A variation of the orbital period of 0.03 hr to an average orbital period of 11.3674 hr is a modulation of

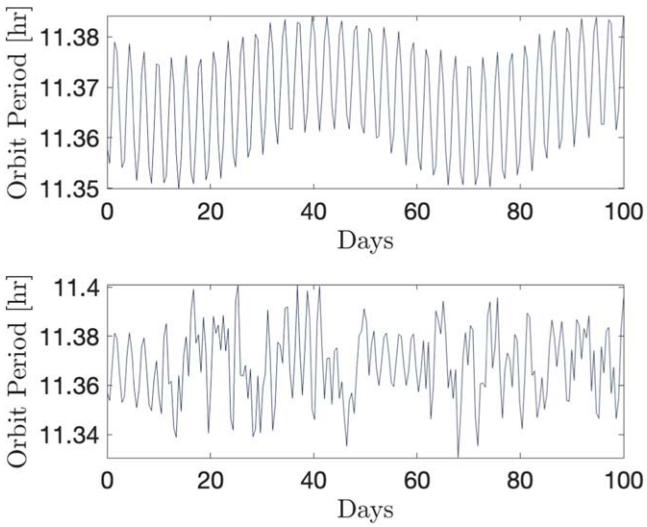

Figure 5 Top: sidereal orbital period for the system with secondary a_s $b_s = 1.3$ and b_s $c_s = 1.1$. Bottom: sidereal orbital period for the system with secondary a_s $b_s = 1.2$ and b_s $c_s = 1.4$.

about 0.26 . This corresponds to a correction to the mean anomaly of about 1°. Extended, high-quality observations have a chance at detecting this error in mean anomaly given suf cient coverage in time. Thus, while orbital-period variations may be hidden from ground-based data, Hera could feasibly detect this phenomenon.

While secular damping is possible in the near future, it is unlikely to have major effects on the system when Hera arrives Meyer et al. 2023b). Thus, Hera may encounter a tumbling Dimorphos, complicating proximity operations. Monitoring of the rotation state with Hera will allow estimates of ω, particularly if the system is in stable libration, but much more uncertain if Dimorphos is tumbling.

There is also a possible detection of a secular trend in orbital period for a short interval after impact that may be due to momentum exchange between the binary and the ejecta. This is discussed further in Section 3.3.3.

2.4. Eccentricity Drop

If Dimorphos entered a tumbling state after impact, this would be accompanied by a relatively rapid decrease in the mutual orbital eccentricity Meyer et al. 2023b). This is driven by an exchange of angular momentum, where the onset of tumbling causes the secondary s angular momentum to decrease on average, resulting in an increase in the orbital angular momentum and corresponding decrease in eccentricity. The magnitude of this decrease depends on the change of libration amplitude in Dimorphos: a large libration amplitude when Dimorphos starts tumbling corresponds to a large drop in eccentricity, whereas a smaller change in libration amplitude corresponds to a smaller drop in eccentricity. So if the libration amplitude after the onset of tumbling is nearly the same as the amplitude prior to tumbling i.e., there is a small change in the secondary s angular momentum), there will not be a large reduction in eccentricity. But if the libration amplitude is much larger after tumbling begins i.e., a large change in the secondary s angular momentum), there will be a large reduction in eccentricity. Thus, while the eccentricity of 0.027 seen shortly after the impact is consistent with a circular preimpact orbit, this value may change over the course of several days, indicating NPA rotation in Dimorphos. Indeed, Scheirich et al. 2024) nd in their dynamical model that after a transient period of about 70 days postimpact, during which the average eccentricity is 0.028 ± 0.005, either a drop in eccentricity to essentially zero or the start of chaotic orbital behavior with onset of tumbling in Dimorphos, is needed to explain their lightcurve data.

3 The Momentum Transfer Enhancement Factor

3.1. Mutual Orbit Change

A key objective of DART as a planetary defense test mission was to determine the momentum transfer to the target body relative to the incident momentum of the spacecraft, which is quanti ed by the momentum transfer enhancement factor, β Cheng et al. 2023), de ned by the momentum balance of the kinetic impact

$$M\Delta \boldsymbol{V} = m\boldsymbol{U} + m(\beta - 1)(\hat{\boldsymbol{E}} \cdot \boldsymbol{U})\hat{\boldsymbol{E}}. \quad (4)$$

Here, M is the mass of Dimorphos, $\boldsymbol{V}$ is the impact-induced change in Dimorphos s orbital velocity, m is DART s mass at impact, is DART s velocity relative to Dimorphos at impact, and $\hat{\boldsymbol{E}}$ is the net ejecta momentum direction. M $\boldsymbol{V}$ is the momentum transferred to Dimorphos, m is DART s incident momentum, and the nal term in the equation is the ejecta s net momentum written in terms of the spacecraft s incident momentum. This de nition of β can be reexpressed as the ratio of the components along $\hat{\boldsymbol{E}}$ of both the momentum transfer and the incident momentum vectors, or $\beta = M(\hat{\boldsymbol{E}} \cdot \Delta \boldsymbol{V})/m(\hat{\boldsymbol{E}} \cdot \boldsymbol{U})$. Since the along-track component of $\boldsymbol{V}$, which is the component along Dimorphos s orbital-velocity direction, $\hat{\boldsymbol{e}}_T$, can be estimated from Dimorphos s orbital-period change, the momentum transfer enhancement factor β is reexpressed in terms of $\Delta \boldsymbol{V} \cdot \hat{\boldsymbol{e}}_T = \Delta V_T$ as

$$\beta = 1 + \frac{\frac{M}{m}(\Delta V_T) - (\boldsymbol{U} \cdot \hat{\boldsymbol{e}}_T)}{(\hat{\boldsymbol{E}} \cdot \boldsymbol{U})(\hat{\boldsymbol{E}} \cdot \hat{\boldsymbol{e}}_T)}. \quad (5)$$

The determination of β for the DART impact Cheng et al. 2023) required estimation of V_T, M, and $\hat{\boldsymbol{E}}$. A Monte Carlo method was used to nd a distribution for V_T consistent with the measured period change incorporating the uncertainties in the Didymos system parameters, such as the ellipsoid axial lengths of the asteroids, the preimpact orbit separation distance between the asteroids, the pre- and postimpact orbital periods, and the net ejecta momentum direction $\hat{\boldsymbol{E}}$. Full two-body numerical simulations Davis & Scheeres 2021) of the coupled rotational and orbital dynamics were used to determine V_T for each sampled combination of input parameters, nding $V_T = 2.70 \pm 0.10\ (1\sigma)$ mm s ^{1}. The mass M of Dimorphos was estimated from the volumes of the ellipsoidal shape models Daly et al. 2023) with assumed values for Dimorphos s density, which was not directly measured by DART. In the Monte Carlo analysis, Dimorphos s density was uniformly sampled between 1500 and 3300 kg m ^{3}. The ejecta momentum direction $\hat{\boldsymbol{E}}$ was found from Hubble Space Telescope HST) and LICIACube observations of the ejecta, which yielded an estimate of the ejecta cone axis direction. This direction is identical to $\hat{\boldsymbol{E}}$ assuming the ejecta plume holds the momentum uniformly, and $\hat{\boldsymbol{E}}$ points toward an R.A. of 138 and a decl. of $+13^{\circ}$ with an uncertainty of 15 around this direction. Combining the inputs for V_T, M, and $\hat{\boldsymbol{E}}$, the dynamical Monte Carlo analysis Cheng et al. 2023) found β as a function of Dimorphos s bulk density ρ_s

$$\beta = (3.61 \pm 0.2)\frac{\rho_s}{2400\ \mathrm{kg\ m^{-3}}} - 0.03 \pm 0.02\ (1\sigma). \quad (6)$$

For a Dimorphos bulk density range of 1500–3300 kg m ^{3}, the expected value of the momentum transfer enhancement factor, β, ranges between 2.2 and 4.9. These β values indicate that signi cantly more momentum was transferred to Dimorphos from the escaping impact ejecta than was incident with DART.

While additional observational data on the Didymos system have been collected in the months following the results shown in Cheng et al. 2023), none of the updates to the aforementioned input parameters for the β analysis have changed suf ciently from their previous values to warrant recalculation of the β estimate. Thus, the next anticipated update to the β result for DART s impact on Dimorphos is expected to come from Hera mission data.

3.2. Heliocentric Orbit Change

The DART impact changed the heliocentric orbit of the Didymos system in addition to changing the mutual orbit of Dimorphos and Didymos. The initial impulse delivered to the system s barycenter was augmented by the momentum carried by the ejecta that escaped the system Jewitt et al. 2023). We de ne the escape criterion as ejecta crossing the Hill sphere of the binary asteroid. The combination of the DART impulse and the momentum transported out of the system by ejecta can be encapsulated in the heliocentric momentum transfer enhancement factor, $\beta_{\odot}$. The $\beta_{\odot}$ value describes the total change in the heliocentric momentum, and therefore the changes to the heliocentric orbit of the Didymos–Dimorphos system caused by the DART mission. Without measuring $\beta_{\odot}$, the total momentum transfer on the entire system can only be constrained through its natural upper bound, namely the local β measured from the change in Dimorphos s orbit. Since some ejecta may stay trapped in the binary system, $\beta_{\odot}$ cannot exceed β. Given the short postimpact observation arc at the time of this writing, a measurement of $\beta_{\odot}$ is not yet possible Makadia et al.

Table 3
Estimated Accuracy for Retrieved $\beta_{\odot}$ for Various Future Observational Campaigns

Scenario	$\beta_{\odot}$	SNR
Five Occ. 2024)	3.212	4.850
Five Occ. 2024) + Five Occ. 2027)	3.025	7.835
Five Hera 2027)	3.011	16.747
Five Occ. 2024) + Five Occ. 2027) + Five Hera 2027)	3.031	17.014

Note The target value to be retrieved in these simulations is $\beta_{\odot} = 3$; Occ: stellar occultation measurements; Hera: Hera pseudorange measurements.

2024). However, high-quality astrometry derived from stellar occultations between 2022 October and 2023 March has helped to make strides toward a statistically signi cant $\beta_{\odot}$ estimate.

Observing stellar occultations is one of the most accurate ground-based methods for measuring the on-sky position and directly determining the size and shape of solar system objects Ferreira et al. 2022). However, stellar occultations of <1 km diameter asteroids present their own inherent challenges Souami et al. 2022). The Asteroid Collaborative Occultation Research via Occultation Systematic Survey ACROSS) project, funded by ESA in its initial exploratory phase, supports the DART and Hera missions. ACROSS observational campaigns on different continents between 2022 June and 2023 March led to 20 successful stellar occultations by Didymos being recorded, four of which allowed for the detection of Dimorphos. This makes Dimorphos the smallest object ever observed during an occultation campaign Souami et al. 2022). It is worth noting that at the end of the Didymos campaigns, occultation astrometry was fundamental to reach an exceptional orbit quality 50 m uncertainty on the sky plane in 2023 March).

Makadia et al. 2024) investigated whether more occultation data could help speed up the process of determining $\beta_{\odot}$. This was done by directly adding $\beta_{\odot}$ to the list of estimated parameters during the orbit determination process for the Didymos system barycenter. The least-squares orbit determination process naturally gives estimates and corresponding 1 uncertainties for $\beta_{\odot}$ after solving the normal equations. Table 3 shows a summary of future observational scenarios considered for the estimation of $\beta_{\odot}$. The rst row corresponds to a case that assumes ve new monthly occultation measurements between 2024 June and October, before the launch of the Hera spacecraft. The second row corresponds to ve additional occultations in 2027 February–June, while the Hera spacecraft is at the Didymos system. The third row considers just ve additional pseudorange measurements of the Didymos system barycenter. These pseudorange measurements are radar delay measurements of the system barycenter taken from tracking data of the Hera spacecraft. Finally, the last row is the combination of all previous scenarios. For additional justi cation of the number and types of these observations, as well as the full methodology behind estimating $\beta_{\odot}$, the reader is referred to Makadia et al. 2024).

The highest signal-to-noise ratio SNR) for $\beta_{\odot}$ naturally comes from the case with the highest number of future high-accuracy observations. However, the more interesting result is that a statistically signi cant estimate of $\beta_{\odot}$ could be generated through additional occultation observations even before the launch of the Hera spacecraft. This scenario is contingent on successful observations from the stellar occultation measurement campaigns in the second half of 2024.

There is, therefore, a clear bene t from follow-up stellar occultation observations, certainly in 2024. The ACROSS collaboration plans to organize dedicated occultation campaigns to observe those events. We predict that the uncertainty of the current orbit of Didymos propagated to the beginning of its observability period in 2024 is only ≈1 Didymos body radius. This means that a small number of observers on the ground can lead to a successful occultation event. Following similar plans to the 2022–2023 campaigns, the ACROSS collaboration will be deploying some of its instruments for the 2024 campaigns and will be interacting with the amateur community to ensure the best coverage of the best events. A rst positive detection in 2024 will then provide the accuracy needed for successful stellar occultation campaigns that capture the events that will follow. As mentioned above, if successful, these 2024 occultations should already provide an SNR of ≈5 by the end of next year. Given additional measurements from the Hera spacecraft, this SNR can then jump to ≈17 in 2027.

3.3. The Dynamical Effects of DART-produced Ejecta on the Didymos System

Here we discuss and quantify the dynamical effects that DART-produced ejecta have on the dynamics of the Didymos system.

3.3.1. Ejecta Mass Estimates

Postimpact observations have provided estimates about the mass of the ejecta produced by the kinetic impact of DART on Dimorphos. As reported in Table 4, the observations are in agreement within an order of magnitude around $\sim 10^7$ kg. Studies based on observed ejecta quantify the mass of a subgroup of ejecta, i.e., leaving the Didymos system up to 2–3 weeks after the DART impact, or within a certain size range. Also, some studies i.e., Gudebski et al. 2023; Jewitt et al. 2023; Roth et al. 2023) assume a lower system density compared to the latest estimates Table 2). In addition, many observations have preferred sensitivity to speci c particle sizes e.g., of order millimeter in diameter), likely missing ejecta in the full particle size range. This implies that numbers in Table 4 likely represent lower-bound values.

The total quantity and mass of ejecta can be estimated by comparing observations to numerical models of dust dynamics and dispersal taking into account a distribution of ejection velocities and particle sizes as well as both gravity and solar-radiation pressure. Such estimates for the total quantity and mass of ejecta vary widely, as summarized in Table 4. The particle sizes of this material probably extend from micrometers into the boulder size regime Cheng et al. 2020, 2022).

Figure 6 shows two examples of ejecta evolution in time. In these cases, the total ejecta mass is $\sim 6 \times 10^6$ kg Moreno et al. 2023) and $\sim 1.5 \times 10^7$ kg Ferrari et al. 2024), respectively. Both models resolve the dynamics of the ejecta fragments as they evolve after the DART impact but starting from different assumptions regarding their initial state. In more detail, both works consider particles in the range of micrometers to centimeters, but Moreno et al. 2023) use a broken power law with index 2.5 for particles smaller than 3 mm, and 3.7 for larger ones, while Ferrari et al. 2024) use a single power law with index 2.7. Also, Moreno et al. 2023) initialize the

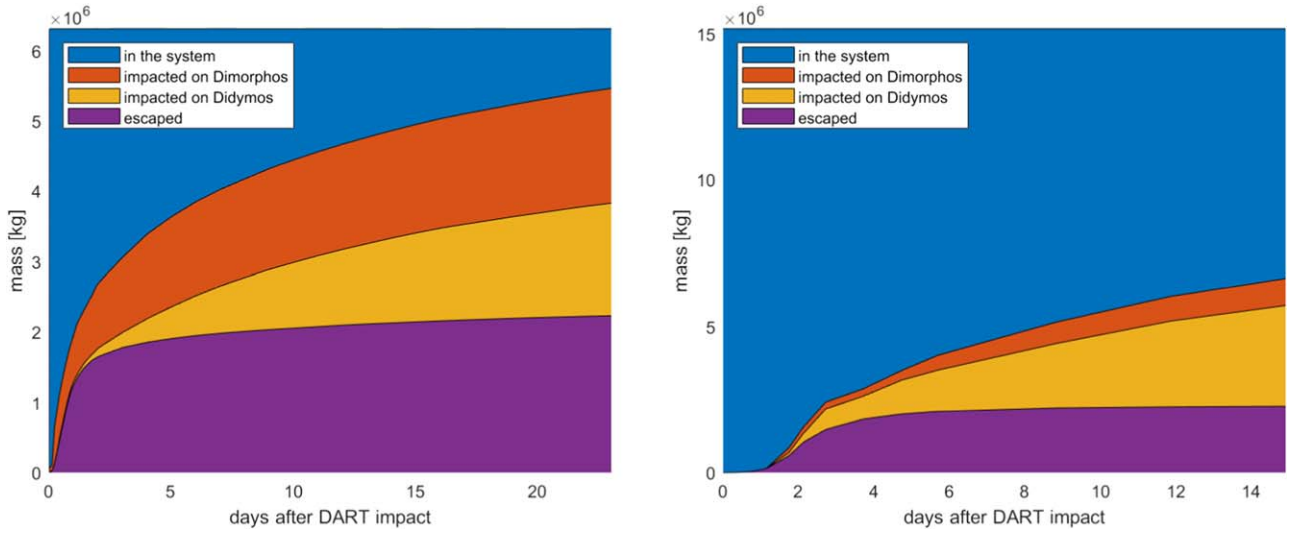

Figure 6 Evolution of ejecta mass in time showing mass escaped from the system versus the mass that remains in the system, either by orbiting about it labeled "in the system") or after reimpacting on Didymos Dimorphos. The colored regions indicate the amount of mass that belongs to each subgroup at each time: i.e., 100 of the mass at $t = 0$ is "in the system," while some mass is being lost to impact on Didymos Dimorphos, or to escape the system, as time progresses. Left: Moreno et al. 2023). Right: Ferrari et al. 2024).

Table 4
Estimates of the Total Ejecta Mass from Observations and Constrained Numerical Simulations

Total Mass kg)	Notes	Reference
4.2×10^6	numerical simulations preimpact)	Moreno et al. 2022)
6.8×10^6	observations, visible, w HST integrating under a differential size–frequency distribution t to tail pro les)	Li et al. 2023)
$1.3–2.2) \times 10^7$	observations, visible, w UNISTELLAR network	Graykowski et al. 2023)
$0.9–5.2) \times 10^7$	observations, millimeter wave, with the Atacama Large Millimeter submillimeter Array	Roth et al. 2023)
5.2×10^6	observations, visible, w HST mass of slow-boulder population alone)	Jewitt et al. 2023)
9.4×10^6	numerical simulations constrained by HST observations in Li et al. 2023)	Moreno et al. 2023)
$1.1–5.5) \times 10^7$	numerical simulations constrained by HST observations in Li et al. 2023)	Ferrari et al. 2024)
$1.7–4.3) \times 10^7$	numerical simulations constrained by LICIACube observations in Dotto et al. 2024)	Raducan et al. 2024a)
$0.65–4.1) \times 10^7$	point-source scaling from numerical simulations constrained by LiciaCube observations in Dotto et al. 2024)	Cheng et al. 2024)
$1.7–2.2) \times 10^7$	numerical simulations constrained by HST observations in Li et al. 2023)	Kim & Jewitt 2023)
$4.5 \pm 3.7) \times 10^6$	analytic arguments from observed postimpact period change constrained by ground-based observations in Naidu et al. 2024; Scheirich et al. 2024)	Section 3.3.3 of this work

Note The former are limited to observed ejecta i.e., within a certain range of sizes, or within a certain time span), while the latter are limited by model assumptions i.e., size range and distribution of ejecta).

velocity of ejecta particles using a combination of an isotropic distribution equal to the escape speed from Didymos) and a power law with index 0.5, while Ferrari et al. 2024) investigate velocity power-law distributions with the index between 0.4 and 1. Both cases show the amount of mass contributing to the early tail escaped) and the ejecta mass that remains in the Didymos system, either orbiting about it labeled "in the system") or impacted on Didymos Dimorphos. Both cases provide a similar estimate of escaped mass after 15 days $\sim 2.15–2.27) \times 10^6$ kg), whereas the largest difference is given by the mass that remains in the system by that time.

The estimates above provide a range of values for impacted mass on Didymos Dimorphos after 15 days between $\sim 2.8 \times 10^6$ and $\sim 4.4 \times 10^6$ kg. Reaccreted mass increases in time, potentially leading to nonnegligible modi cation of the mass and inertial properties of the asteroids. This affects the dynamics of the binary system, as discussed in Section 3.3.3 below.

3.3.2. Effect of Impact Site Curvature and Geometry

Both the ejecta cone edge s mass and geometry play a role in determining β, as well as the dynamical evolution of the ejecta in the system. LICIACube s LUKE and HST images captured a relatively wide cone Li et al. 2023; Dotto et al. 2024). The HST image analysis derived the opening angle as $125° \pm 10°$ under the assumption that the ejecta cone was axisymmetric Li

et al. 2023). We expand this earlier work to apply both LICIACube LUKE and HST images to further constrain the ejecta cone edge geometry using the different view planes of these observers. The cone axis was found to point toward R. A., decl.) = 141.°0 ± 4.°0, 20.°2 ± 8.°0) in the J2000 equatorial frame, which is consistent with the DART spacecraft s incoming direction to within 20° Hirabayashi et al. 2024). The analysis determined the ejecta cone was elliptical in opening angle, i.e., its intersection with a plane perpendicular to its axis formed an ellipse. The narrower cone opening angle in the direction of the ellipse s shorter axis was 94.°8 ± 5.°4 and the wider cone opening angle in the direction of the ellipse s longer axis was 133.°3 ± 9.°2. The latter direction is favored along Dimorphos s north–south direction but was rotated by 26.° 0 ± 16.°0 counterclockwise from the north about the cone axis in the Dimorphos- xed frame. This condition results in ejecta from high latitudes tending to depart from Dimorphos more shallowly relative to a plane normal to the along-track direction than from lower latitudes. This ejection angle variation indicates the contribution of Dimorphos s higher curvature along its body-frame north–south direction compared to its east–west direction Hirabayashi et al. 2024). Further assessments applying the derived ejecta geometry analysis and numerical simulations of the DART impact reveal that the curvature of the target led to a reduction of the along-track momentum transfer enhancement Raducan et al. 2024a; Hirabayashi et al. 2024).

3.3.3. Binary Hardening Effect

Most of the dynamical modeling of the Didymos system after the DART impact has focused on understanding the system s excitation in the F2BP; however, the complete Didymos system immediately and for some time after the impact consisted of many interacting bodies. Indeed, preimpact numerical simulations predicted that a large amount of debris could be generated from the impact e.g., Fahnestock et al. 2022; Ferrari et al. 2022; Rossi et al. 2022; Tancredi et al. 2023). Observations from LICIACube and nearly simultaneous space-based and ground-based observations demonstrated that large amounts of debris were generated at the time of impact e.g., Graykowski et al. 2023; Kareta et al. 2023; Li et al. 2023). Follow-up observations from both space- and ground-based observatories have also seen a persistent tail that has lasted for over 250 days e.g., Li et al. 2023; Moreno et al. 2023). Finally, dynamical models of the postimpact two-body system indicate a reduction in the orbital period of 34 ± 15 s Naidu et al. 2024) and 19 ± 6 s over the rst ∼15 days Scheirich et al. 2024; 1 uncertainties). These aspects motivate considering whether the binary was "hardened," i.e., the binary s orbital energy decreased due to gravitational interactions with the debris, so that the lost orbital energy was transferred to either escaping unbound debris or transferred via collisions into the rotation states of Didymos and or Dimorphos.

The bound ejecta would have formed a thick, broad, evolving annulus about the Didymos–Dimorphos system Ferrari et al. 2022). Collisions between debris particles would only be important if the debris cloud were a very thin and narrow annulus, e.g., ∼100 m wide Stewart et al. 1984) assuming a very thin annulus given ejecta mass on the order of 10^7 kg see Table 4) and a typical particle of about 1 mm diameter with a density of 3 g cm ^{3} Moreno et al. 2023). Instead, the bound ejecta disk must have been very broad, extending from the binary orbit ∼1.2 km) out to the Hill sphere of the system Jewitt et al. 2023; Kareta et al. 2023; Li et al. 2023). Furthermore, the disk will hardly be thin since the debris was ejected in a cone geometry Deshapriya et al. 2023; Li et al. 2023; Dotto et al. 2024), placing debris on a range of inclinations relative to the Didymos–Dimorphos orbital plane. Thus, the postimpact debris cloud was very diffuse, particle–particle collisions were rare, and the orbits of debris particles evolved due to other processes.

Due to interactions both with the binary gravitational dynamics and solar-radiation pressure, ejecta are unlikely to settle onto stable orbits Ferrari et al. 2022; Rossi et al. 2022). Instead, the particles will have strong interactions at their orbital pericenters with Didymos and Dimorphos. Each encounter will scatter the particles onto new orbital planes and create a random walk in the semimajor axis, eccentricity, and inclination of the ejecta orbits Jacobson & Scheeres 2011; Rossi et al. 2022). Furthermore, solar-radiation pressure will strongly perturb particle orbits and will quickly unbind particles less than about 1 mm in diameter Ferrari et al. 2022; Tancredi et al. 2023). However, larger particles are likely to persist for a longer time that depends on their size, consistent with the observed long-lasting tail Moreno et al. 2023).

The population of larger particles in the Didymos system will decay with time due to loss onto heliocentric orbits and collision with Didymos and Dimorphos, as shown in Figure 6. While particle–particle collisions are unlikely to play a signi cant role in the evolution of their orbits, a signi cant number fraction of the particles will likely collide with Didymos or Dimorphos see Figure 6). In other words, each particle s residence time in the Didymos system depends on its properties radius, density, etc.) and ejection location and velocity, but not on the other particles. This means the particle loss rate is proportional to the total number of particles N remaining in the system, i.e., $\frac{dN}{dt} \propto -N$, which has the well-known solution of exponential decay, $N = N_0 e^{-(t-t_0)/\tau}$, where τ is the exponential decay timescale, N_0 is the initial number of particles, and t_0 is the time of the DART impact. Using this exponential decay model, the timescale for clearing the Didymos system is proportional to the timescale associated with the scattering events that occur near the pericenter of each particle s orbit. Thus, τ is proportional to a characteristic ejecta orbital period P_e: $\tau \propto P_e$.

Ejecta will have a range of Didymos–Dimorphos system orbital periods P_e depending on their ejection velocity after the DART spacecraft impact. All ejecta not lost immediately to heliocentric orbit have ejection speeds less than the escape speed from the Didymos system i.e., 24 cm s ^{1}; Tancredi et al. 2023). For ejecta launched with very low speeds relative to Dimorphos, the ejecta period is similar to the mutual orbital period of Didymos–Dimorphos $P_e \approx 0.5$ days. Other bound ejecta will have been launched on orbits with apocenters Q_e very close to the Didymos–Dimorphos system Hill radius r_H at the time of the DART impact

$$r_H = r_D \left(\frac{m}{3M_\odot} \right)^{1/3} = 73 \text{ km}, \quad (7)$$

where $r_D = 1.1$ au is the heliocentric distance of the Didymos system at the time of the DART impact Rivkin et al. 2021), $m = 5.3 \times 10^{11}$ kg is the Didymos–Dimorphos system mass

Table 2), and $M_{\odot} = 2.0 \times 10^{30}$ kg is the Sun s mass. Debris with apocenters closest to the Hill radius are very easily perturbed by solar-radiation pressure onto heliocentric orbits, contributing to the long-lasting tail, and so they do not interact much with the Didymos–Dimorphos system. However, stably bound debris Q_e 0.5 r_H, i.e., with apocenters well within the Hill radius, motivated in part by studies of the stability of irregular satellites; Nesvorný et al. 2003) will have orbital periods of about P_e 15 days assuming pericenters q_e near the Didymos–Dimorphos separation distance $q_e \approx a = 1.2$ km. These estimates set a clearing timescale τ on the order of days to weeks, which is consistent with both the more detailed numerical experiments shown in Figure 6 and is consistent with the observed mutual orbital-period change timescale Scheirich et al. 2024).

The effect of this exponentially decreasing population of debris on the dynamics of the Didymos–Dimorphos system is the dynamical hardening of the binary due to exchange of angular momentum of the binary system with the escaping ejecta, potential small impulses upon the binary components from accretion impact events, and to a much-lesser extent an increase of the system mass due to that same accretion. To test whether these processes may be responsible for the observed change in the Didymos–Dimorphos orbital period, we calculate an independent estimate of the amount of ejected mass needed to effect that change and compare it to observed estimates of the ejected mass.

First, using a Keplerian model for the Didymos–Dimorphos system, we determine how much the orbital angular momentum of the binary changed given the observed period change

$$\Delta L = \frac{L}{3P}\Delta P, \tag{8}$$

where $L = m_s\sqrt{Gma}$ is the initial angular momentum of the Didymos–Dimorphos circular orbit, $m = m_p + m_s$ is the combined mass of Didymos m_p and Dimorphos m_s, and we assume the reduced mass can be approximated by the mass of Dimorphos. The change in angular momentum of the binary L is the opposite of the change in the angular momentum of the particle orbits L_e, which is the difference in angular momentum of the ejected particles on their nal parabolic orbits and their elliptic orbits immediately after ejection. Thus, the change in the angular momentum of the binary is

$$\begin{aligned}\Delta L &= -\Delta L_e \\ &= -m_e(\sqrt{2Gma_e(1 - e_e)} - \sqrt{Gma_e(1 - e_e^2)}),\end{aligned} \tag{9}$$

where m_e is the mass of ejected material that is not lost immediately to heliocentric orbit. To good approximation, the Didymos–Dimorphos orbit is circular and since most of the ejecta were launched off the leading face of Dimorphos, the ejecta would have an apocenter exterior to the Didymos–Dimorphos orbit and a pericenter similar to the semimajor axis of Dimorphos s orbit: a_e 1 $e_e) = a$. Equations 8) and 9) can then be solved for the initially bound but ejected mass

$$m_e = \frac{m_s}{\sqrt{1 + e_e} - \sqrt{2}}\left(\frac{\Delta P}{3P}\right) = \frac{(9.5 \pm 5.9) \times 10^5 \text{ kg}}{\sqrt{2} - \sqrt{1 + e_e}}, \tag{10}$$

where the mass of Dimorphos is $m_s =$ $4.5 \pm 0.4) \times 10^9$ kg and the postimpact mutual period is $P = 11.3674 \pm 0.0010$ hr see Table 2). The two estimates of the postimpact period change are $P =$ 34 ± 15 s Naidu et al. 2024) and $P =$ 19 ± 6 s Scheirich et al. 2024). Scheirich et al. 2024) caution that their estimate is only a lower limit on the absolute magnitude of the change and that the real change may be slightly higher. If we take these estimates at face value and average them, we estimate the period change as $P =$ 26 ± 16 s. A minimum ejected mass estimate $m_e \gtrsim (2.3 \pm 1.4) \times 10^6$ kg is obtained if the initial ejecta eccentricities are low $e_e \approx 0$). If the ejecta that interact strongly with the Didymos–Dimorphos system i.e., have many pericenter passages) are initially spread out evenly on orbits with apocenters between the Didymos–Dimorphos orbit $Q_e = a_e$ and so $e_e \approx 0$) and half the distance to the Hill radius $Q_e = 0.5$ r_H and so $e_e \approx 0.9$), then the estimated ejecta mass is $m_e = (4.5 \pm 3.7) \times 10^6$ kg. This estimate of the unbound ejecta mass estimate is a similar order of magnitude as other estimates of the ejected mass, although most of those are for the unbound component see Table 4). Notably, it is very similar to the comparable fallback mass of 5.4×10^6 kg estimated from analysis of HST images Kim & Jewitt 2023).

Next, we consider the change in angular momentum of the binary system due to reimpacting mass. This is very similar to the original DART experiment except that the debris is not likely striking Dimorphos only in the along-track direction. Irrespective of the momentum transferred from colliding ejecta to the binary components, in a Keplerian model, growth in the binary mass changes the binary orbital period according to $P =$ P m $2m$). Using the same values as above, the change in the system mass would need to be about 0.13 or $m = 6.6 \times 10^8$ kg to explain the observed period change. This is much more ejecta mass than other independent estimates suggest. Thus, mass reaccretion will play only a small role in any detected period change.

However, reaccretion will also deliver angular momentum to the orbit due to small torques associated with each impact event. If these torques are truly random, then they will cancel out, but if not, then this reimpacting ejecta material may change the orbital period. In this case, the change in the angular momentum due to reimpacting material can be estimated as

$$\Delta L = m_r\sqrt{Gma_r(1 - e_r^2)}, \tag{11}$$

where a_r and e_r are the average semimajor axis and eccentricity of ejecta material prior to reimpact, respectively, and m_r is the reimpacting mass that contributes to the nal change in angular momentum of the binary note that this reimpacting mass is a lower limit since some mass might have reimpacted that did not change or even increased the angular momentum of the binary, canceling out yet other mass that did decrease the binary angular momentum). Equations 8) and 11) can then be solved for an estimate of minimum reaccreted mass, then

$$m_r \geqslant m_s\sqrt{1 + e_r}\left(\frac{\Delta P}{3P}\right) = \sqrt{1 + e_r}(9.5 \pm 5.9) \times 10^5 \text{ kg}, \tag{12}$$

where we have again asserted that the pericenter of the reimpacted debris is similar to the semimajor axis of the

Didymos–Dimorphos system. If the debris is mostly circular $e_r \approx 0$), then the minimum reimpacting mass is $m_r \geqslant (9.5 \pm 5.9) \times 10^5$ kg. Since much of the debris is likely placed on eccentric orbits and some of the debris is likely to collide with Didymos or Dimorphos to increase the binary orbital angular momentum, we emphasize that the required mass of reaccreted debris is likely much higher than this estimate. Many independent estimates of the ejected debris are on order 10^6 kg, so it may be reasonable that a similar mass was lofted but ultimately reaccreted by Didymos and Dimorphos. This calculation establishes that such a large mass of debris would be necessary to fully explain the observed period change of the binary, but whether reaccreted mass would ultimately add or remove angular momentum requires future detailed simulations. Thus, reaccretion and ejection likely play a role in the observed postimpact binary hardening of the system.

From these simple considerations, we nd that the cloud of nonescaping ejecta should dissipate on an exponential timescale and gravitational interactions with that cloud would lead to angular momentum transfer that would ultimately harden the orbit of the Didymos–Dimorphos system due to slowly escaping material. These considerations are consistent with both observations of a mutual orbital-period change of the system as well as independent estimates of the amount of debris created and its evolution. Future work should examine the many-body dynamics of the ejecta cloud and binary system more fully. The angular momentum transfer between the bound ejecta cloud and the binary system appears measurable, and so this is an independent constraint on the amount of slow ejecta created by the DART impact.

The previous analysis has implications for β. The negative period change induced by the DART impact appears to be slightly increasing in magnitude over time and therefore the measure of β is also slightly increasing). That is, the "immediate" β is slightly lower than the "eventual" β for this system. This is likely to be true of any binary system when impacting the secondary more or less head on. Although this effect is measurable in this instance, it has a very minimal effect on the nal period change and eventual β. Consider the persistent particles in the system. Among the particles ejected by the DART impact, many were launched from the surface of Dimorphos at speeds less than the escape speed of the system. This resulted in particles orbiting in the system for some time after the impact. These persistent particles can reach a number of outcomes: they can reimpact Dimorphos, transfer impact onto Didymos, escape the system after close encounters with Dimorphos, or nd a stable orbit within the system. Finding a stable orbit in the system is very unlikely for most of the particles but we include this possible outcome for completeness. Particles that have close encounters with Dimorphos are ef cient at increasing the period reduction for Dimorphos and can explain the continuous period change. Such change appears to be a product of Dimorphos being in a binary system and it is possible that a single asteroid would not experience a similar phenomenon. This is one instance where the DART impact diverges from the case wherein a single asteroid is impacted. An impact into a single body would still result in a fraction of persistent particles but this would likely be a much smaller fraction than what we see at Dimorphos. The particles ejected from a single body below its escape speed would mostly) be on reimpact trajectories with the body. Some may orbit the single body but they could not escape the system via close encounters with a secondary body. This is a fundamental difference between two-body systems and three-body systems, where three-body systems often eventually eject the smallest body and two-body systems have no ability to do so without external perturbation.

4 Shape and Structure Effects

Detailed images from DRACO, DART s camera, documented unique geologic features of both Didymos and Dimorphos Daly et al. 2023). This binary system, or at least its satellite, is likely made of gravitational aggregates rather than monolithic bodies, given the observed unique surface morphology and shapes Daly et al. 2023). The Didymos binary system is a member of the most common class of binary systems, in which the satellite is much smaller than its primary a few percent of the system s mass; Pravec et al. 2006). Binary systems should form and evolve due to mass transport between gravitationally bound bodies driven by events changing their dynamical and structural con gurations such as impacts, tidal effects, and solar radiation. Didymos looks like a top shape but not exactly so; compared to Ryugu Watanabe et al. 2019) and Bennu Barnouin et al. 2019), the very oblate shape likely resulted from various mechanisms related to its fast spin. The oblate shape of Dimorphos at least prior to impact) is at odds with the expectation of a prolate shape Walsh & Jacobson 2015) and is an important constraint on formation models. Structural modi cations during the system s evolution also change the system s dynamical behavior. This section describes the current state-of-the-art understanding of the binary system s structural stability and how it contributes to dynamical evolution.

4.1. Structural Properties and Stability of Didymos

4.1.1. Preencounter Understanding Constrained by Shape and Spin State

Prior to the DART encounter, the binary system s physical characteristics were primarily inferred from ground-based observations. Photometric and radar observations estimated Didymos s spin period to be 2.2600 ± 0.0001 hr, and the mutual orbit elements yielded bulk density estimates of $\rho_p = 2170 \pm 350$ kg m ^{3} and 2370 ± 300 kg m ^{3} for Didymos see Table 2). The radar-derived shape model gave Didymos s dimensions along the principal axes as 832 ± 6) $\times$ 838 ± 6) $\times$ 786 ± 10) m Naidu et al. 2020).

The preencounter understanding implied Didymos possesses mechanical strength, ensuring both interior and surface structural stability Hirabayashi et al. 2022). Numerical simulations using discrete-element modeling provide two avenues to maintain Didymos s structural integrity at its rapid spin rate, i.e., through either global weak cohesion or strong mechanical core strength e.g., Zhang et al. 2021; Ferrari & Tanga 2022). Assuming a homogeneous rubble-pile structure with various potential boulder size distributions, Didymos s minimum required bulk cohesive strength is estimated to be $\sim$11–17 Pa for $\rho_p = 2170$ kg m ^{3} and $\sim$2–13 Pa for $\rho_p =$ 2370 kg m ^{3} Zhang et al. 2021). Alternatively, if Didymos s strength distribution is heterogeneous, a cohesionless external layer can suf ce for structural stability, provided that over half of the interior possesses strong mechanical strength or rigidity Ferrari & Tanga 2022).

4.1.2. Postencounter Understanding Constrained by Shape and Spin State

By analyzing the close-encounter images obtained from DRACO, Didymos s dimensions were updated to $819 \pm 14) \times 801 \pm 14) \times 607 \pm 14)$ m Barnouin et al. 2024). This shape is remarkably smaller and more oblate than the radar shape model, yielding a signi cantly higher bulk density of 2790 ± 140 kg m ^{3} see Table 2). Material cohesive strength is no longer a crucial requirement for maintaining Didymos s interior structural stability at the spin period of 2.26 hr, provided its material internal angle of friction a measure of friction between particles that opposes shear and that is typically similar in value to the macroscopic "angle of repose") is larger than ∼40 Zhang et al. 2017; Agrusa et al. 2024). For a lower friction angle of ∼35 , interior cohesion of ∼10 Pa is still needed to prevent internal deformation Agrusa et al. 2024; Barnouin et al. 2024). Some surface regions on Didymos have slopes exceeding 45°, indicating that a small cohesive strength of ∼1–2 Pa might be present on Didymos for maintaining the stability of these high-slope regions Barnouin et al. 2024). The surface cohesive strength might need to exceed the static estimate in order to maintain the structural stability of the surface during the impact of ejecta resulting from the DART impact see Section 4.1.4).

If the interior does not possess a proper level of mechanical strength, internal failure of a rubble-pile body may occur during a spin-up process driven by YORP torque Hirabayashi et al. 2015; Sánchez & Scheeres 2018). This could explain the pronounced oblateness observed in Didymos s current shape. Conversely, high internal strength coupled with low surface strength might induce surface mass transport, which is hinted at in the DRACO images Barnouin et al. 2024). The possibility of shedding these mobile surface materials, followed by their gravitational accumulation in orbit around Didymos, offers a plausible explanation for the origin of Dimorphos see Section 4.2). It is likely that Didymos s structural properties lie between these two extremes, allowing it to exhibit both interior- and surface-failure behaviors at fast spin Barnouin et al. 2024). Internal failure could give rise to a density distribution heterogeneity with a less-dense core, akin to the case of Bennu Zhang et al. 2022). The upcoming gravity- eld measurements and radio experiments to be conducted by the Hera mission Section 5) will provide the means to con rm the existence of such heterogeneity and quantify the interior structure s influence on the dynamics of the binary system.

4.1.3. Reshaping of Didymos

Due to Didymos s fast spin, it is possible that the body is sensitive to structural failure at present e.g., Hirabayashi et al. 2015; Nakano et al. 2022). Small perturbations, such as ejecta from the impact site on Dimorphos striking Didymos at various speeds, could thus trigger a reshaping process, wherein its equatorial radius increases while its polar radius decreases, resulting in a more oblate shape Hirabayashi et al. 2022; Nakano et al. 2022). Such reshaping would perturb the mutual gravitational elds and therefore the mutual dynamics between the bodies. Studies prior to the DART impact demonstrated that Didymos s reshaping under constant volume i.e., no mass change due to ejecta accretion) always reduces the orbital period of Dimorphos owing to an increased J_2 moment Nakano et al. 2022; Richardson et al. 2022). It was found

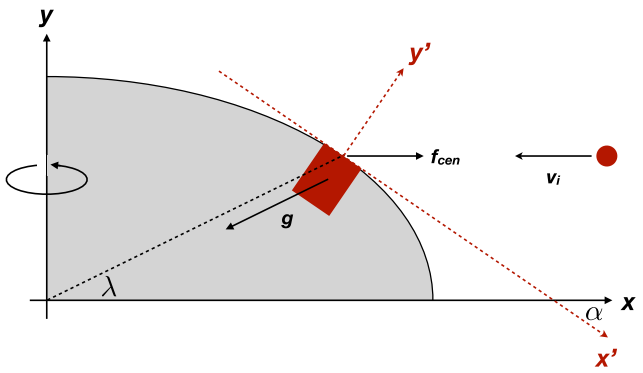

Figure 7 Scheme for positioning boxes on the surface of an ellipsoidal body. The x –y coordinates represent the rotating frame of reference of the simulation box. The angles λ and α represent the latitude and the surface slope, respectively, in the inertial frame. The vectors $\boldsymbol{g}$, $\boldsymbol{v}_i$, and $\boldsymbol{f}_{\rm cen}$ are gravity, the projectile s impact velocity, and centrifugal force at the surface, respectively.

that a 0.7 m of change in the polar radius leads to an orbital-period change of 7.8 s, which exceeds the DART Level 1 measurement requirement i.e., 7.3 s; Rivkin et al. 2021). This implies that the β estimation process likely needs to account for the effect of Didymos s reshaping when the magnitude of reshaping exceeds 0.7 m, as otherwise, the β value could be overestimated Nakano et al. 2022; Richardson et al. 2022).

Importantly, if Didymos s reshaping were to occur, its spin period would change as its moment of inertia is modi ed. This potentially provides a means to constrain the magnitude of reshaping, as the spin period change can be precisely measured. However, current measurements show that the spin period has been constant since preimpact, with an uncertainty of 1 s at the 3 level J. Ďurech & P. Pravec 2024, in preparation). This suggests that Didymos s reshaping likely did not occur, possibly due to either the impact-related perturbations not being strong enough to trigger reshaping or the asteroid s structure being relatively resistant to reshaping, allowing it to withstand the perturbations. Therefore, it is reasonable to conclude that the β estimation process currently does not need to account for the effect of Didymos s reshaping.

4.1.4. Surface Strength Constrained by Ejecta Impacting on the Surface

As noted earlier, the DART impact generated a lot of debris, so much so that Dimorphos acquired a long-lived tail that transformed it into an active asteroid. Part of this debris very likely landed on Didymos, but no appreciable change in either its shape or dynamics was observed Section 4.1.3). This implies Didymos s surface was strong enough to withstand such impacts. Here we simulate this process using an oblate spheroid of homogeneous density and strength rotating around its shortest axis to represent Didymos Figure 7), updating the work of Hirabayashi et al. 2022) who assumed a spherical shape. We simulate impacts onto surface elements of Didymos to infer a lower limit for its cohesive strength. Impact simulations were carried out using Granular Dynamics Code–Impacts, a soft-sphere discrete-element method code for simulating impacts at various velocities Sánchez & Scheeres 2018; Ballouz et al. 2021). Within the method, each particle is treated as an individual object that follows the laws of classical mechanics and moves under the influence of the forces imposed on it. Particles interact with each other through

repulsive soft potentials and a collision is said to have occurred when the distance between the center of any two particles is less than the sum of their radii. The normal repulsion force is provided by a spring linear or Hertzian) and dashpot model. Friction forces are implemented through tangential springs whose response is truncated to satisfy the local Coulomb criterion. Rolling and twisting friction can also be implemented to mimic the behavior of nonspherical particles for details see Ai et al. 2011; Sánchez & Scheeres 2011; Schwartz et al. 2012; Sánchez & Scheeres 2016).

Following Hirabayashi et al. 2022), we place $1 \times 2 \times 1$ m boxes, with periodic boundary conditions, on the surface of the oblate spheroid and ll them with 60,000 spherical grains with a uniform distribution of diameters between 2 and 3 cm to a height of ≈84 cm. We assume Didymos has a bulk density of 2950 kg m ^{3}, and the particle density is set to 4916.67 kg m ^{3} so that the bulk density of the box is the same as that of Didymos. Note that, as investigated by Sunday et al. 2022), boundary effects could affect the outcomes of the simulated impact scenarios. In our case, the periodic boundary conditions eliminate the effects of the walls and emulate an in nite granular surface on which particles of the ejecta eld will impact Radjai 2018). If we tried to eliminate boundary effects by increasing the size of the system so that sound waves do not reach the border, we would need a granular bed of $4 \times 4 \times 2$ m 95 of energy is dissipated every ≈2 m; Sánchez et al. 2022); this would incrementally increase the simulation time by a factor of 32. If we add a reduction in the particle size to just half of what we have, that time would increase fourfold. Together they would increase the computation time by a factor of 128 ≈1 yr per simulation) making them impractical with the current computational facilities and code. Furthermore, since it is the impact of many particles of an ejecta curtain that we seek to simulate, ours is an appropriate representation of a realistically much larger system as it would be unlikely that only one impact takes place in isolation of all others.

The angle of friction of this granular bed is set to ∼35 , a common value for geological regolith and also what was estimated for asteroid Dimorphos Robin et al. 2024). These boxes are placed in the northern hemisphere of the spheroid, along the longest meridian and at latitudes of 0 , 15 , 30 , 45 , 60 , and 75 . Cohesive strength was tested at 0, 1, 2, 3, 4, 5, 10, 15, and 20 Pa. The impact speed was kept at 1 m s ^{1} in the inertial frame Yu & Michel 2018), but it changes in the body frame depending on the latitude of impact due to the rotation of the asteroid, which provided a horizontal velocity component up to 0.32 m s ^{1}). All impacts were set to be perpendicular to the axis of rotation in the inertial frame of reference see Figure 7). Each granular bed was impacted ve times by identical projectiles at the same speed at 2 s intervals. The rst projectile is always placed just above the surface of the granular bed and then shot. After 2 s, the same projectile is repositioned outside of the box and reshot. The process is repeated four times to complete ve impacts. In most cases, this 2 s time interval was enough for the projectiles to either stop due to the collision or simply pass through the granular material if the previous impact had already fluidized it. A granular material is said to be fluidized when the kinetic energy of the system is comparable to its potential energy. The projectiles were aimed to a point in the center of the box, 10 cm below the surface. Note that though the simulation has periodic boundary conditions, the projectile is impervious to them and simply sees the granular bed and not the containing box. We do this because of two reasons, one computational and one physical. Computationally, given that four out of the ve projectiles start their motion from outside the box, this would have brought complications for the algorithms. Physically, if the granular bed is already so fluidized that a projectile goes through the boundary after the impact, it will not have made a difference in our assessment of whether or not the bed was already fluidized. If the granular bed is not fluidized and the projectile merely bounced on the surface, most of its energy would have been already dissipated in the rst impact; a second impact after crossing the boundary would not have done anything signi cant.

As the simulation boxes themselves change their orientation with respect to the body frame depending on their latitude, we need to calculate some angles and distances so that gravitational, Coriolis, and centrifugal forces are adequately calculated see Figure 7). So, if a, b, and c are the dimensions of the semiaxes of the spheroid, $a > b > c$. The distance r between the body center and surface at a given latitude λ is

$$r(\lambda) = \frac{ac}{\sqrt{a^2 \sin^2 \lambda + c^2 \cos^2 \lambda}}, \tag{13}$$

which means that the radius of rotation of any box the distance between the box and the axis of rotation of the body) is $r \cos \lambda$. Differentiating the ellipse equation see Figure 7), the slope of the curve i.e., the meridian of the ellipsoid) is

$$\alpha = \arctan \frac{-cr(\lambda)\cos \lambda}{a\sqrt{a^2 - r^2(\lambda)\cos^2 \lambda}}, \tag{14}$$

which is a negative number. The angle of the gravity vector in the rotating frame of reference is $\pi + \lambda$ α and the angle of the centrifugal force is α, where α is the surface slope in the inertial frame. Finally, the angle of the angular velocity vector, for the calculation of the Coriolis force, is π α. These angles are used in the simulation for the calculation of all these forces on each grain.

Figure 8 shows snapshots of the simulated granular bed after being impacted by the nal projectile. With the new constraints, this revised set of simulations shows that a bulk cohesive strength of 3 Pa would be more than suf cient to avoid material flow and any kind of global reshaping of Didymos. This nding, along with those about the needed cohesive strength for structural stability under rotation see above), show that a cohesionless structure is incompatible with the observations. Our results show that asteroid Didymos needs to have a nonzero cohesive strength to be able to maintain its structure intact under rotation and debris impacts. Additionally, and as observed experimentally by Murdoch et al. 2017b) and Walsh et al. 2022) during the OSIRIS-REx mission TAGSAM event, cohesionless systems are more easily penetrated and fluidized in weaker gravitational elds compared to Earth s Zacny et al. 2018).

Given that we have used only spherical particles, the amount of geometrical interlocking also called geometrical cohesion), and its contribution to shear strength, is diminished Govender & Pizette 2021). Even if rolling friction is implemented, it is dif cult to establish how similar its effect is to interlocking to avoid fluidization or granular flow. This implies then that the exact amount of cohesive strength needed to avoid granular

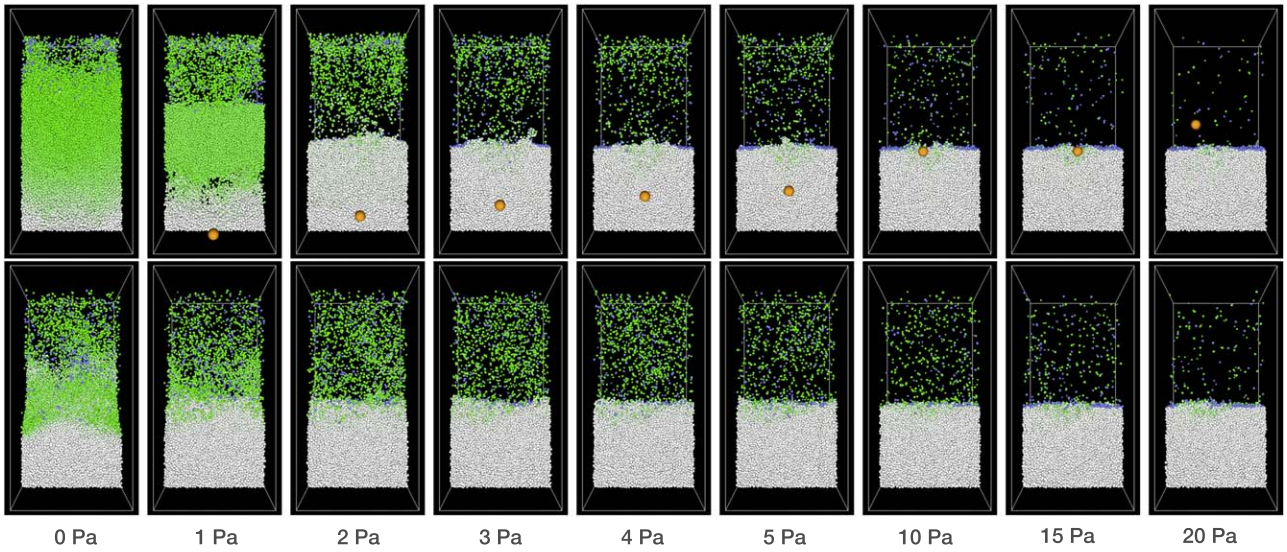

Figure 8 Snapshots of projectile impacts into a granular surface for different levels of cohesive strength. The images are taken 60 s after the last projectile was shot top: $\lambda = 0°$; bottom: $\lambda = 45°$). From left to right, cohesive strength is 0, 1, 2, 3, 4, 5, 10, 15, and 20 Pa. The orange sphere that appears in some of the images is the last projectile. Particles with speeds $> 1 \times 10^{-4}$ m s^{-1} are turned green; blue particles were those on the very surface of the granular bed before the rst impact. The particles in the front half of the box have been made transparent to aid visualization.

flow on the surface of Didymos could be somewhat lower, though still necessary.

4.2. Origin of Dimorphos and Its Preimpact Oblate Shape

Didymos s shape, fast rotation, and geophysical properties suggest that—at some point in the past—Didymos likely exceeded its spin limit, leading to the formation of Dimorphos Walsh & Jacobson 2015; Barnouin et al. 2024; Agrusa et al. 2024). Dimorphos s obliquity being near 180° Rivkin et al. 2021) implies that this spin-up process was dominated by YORP Vokrouhlický et al. 2015), although natural impacts may have played some role as Didymos spends a signi cant fraction of time in the inner main belt Holsapple 2022; Campo Bagatin et al. 2023).

If Dimorphos is indeed a rubble pile with little to no cohesion Barnouin et al. 2024; Raducan et al. 2024a), then Dimorphos likely formed via gravitational reaccumulation outside the Roche limit of Didymos, as the body would not survive a ssion event intact and would naturally be disrupted by tides e.g., Agrusa et al. 2022a). However, Dimorphos s apparent oblate shape is not immediately explained by such a scenario, since gravitational accumulation in a strong tidal environment would tend to create a more prolate shape Madeira et al. 2023; Agrusa et al. 2024; Wimarsson et al. 2024).

Although Dimorphos s unexpected oblate shape is structurally stable at its preimpact orbit and assumed spin period Holsapple & Michel 2006; Sharma 2009), this shape stands in contrast to the measured shapes of other secondaries—either by radar Ostro et al. 2006; Becker et al. 2015; Naidu et al. 2015) or by lightcurve measurements Pravec et al. 2016, 2019)—which tend to be more prolate. Given that DART only saw one hemisphere of Dimorphos and the extent of the b axis was inferred by the geometry of the terminator Daly et al. 2023), it is possible that Dimorphos s true shape is prolate, with a small libration that shifts the illumination so as to mimic an oblate shape. If the true shape is oblate, then this means that Dimorphos either formed with such a shape or longer-term processes such as additional mass-shedding events or natural impacts could have led to an oblate shape. The issue of prolate oblate shape and its implications on the formation and evolutionary processes at work are ongoing topics of study.

4.3. Structural Properties and Potential Postimpact Recon guration of Dimorphos

The high-resolution images of Dimorphos s surface returned by DART exhibited a predominantly blocky texture composed primarily of boulders with diameters in the 0.1–10 m range, indicating a low-cohesion surface structure Barnouin et al. 2024; Daly et al. 2023). If Dimorphos s subsurface and interior share a comparable distribution of boulder sizes, its overall mechanical strength would be notably weak, and its shape and surface morphology could be susceptible to alteration due to the tidal forces exerted by Didymos or potential impacts from external objects.

As a direct result of the DART impact, Dimorphos undoubtedly experienced signi cant resurfacing near the impact site Raducan et al. 2024a). Additionally, indirect downstream effects would likely alter Dimorphos s postimpact morphology on a longer timescale. For example, the impact released signi cant amounts of ejecta Li et al. 2023; Moreno et al. 2023). Any material that was not on an escape trajectory or blown away by solar-radiation pressure can remain bound to the binary system for weeks or months, if not longer Section 3.3.3). A signi cant portion of this material will reimpact Dimorphos at speeds on the order of a few centimeters per second, likely disturbing the surface upon impact Ferrari et al. 2024). Another indirect mechanism for resurfacing is caused by the postimpact excited dynamical state of Dimorphos. Building upon the current understanding of Dimorphos s shape and structural properties, we analyze the likelihood of resurfacing and reshaping behaviors of Dimorphos after the DART impact.

4.3.1. Tidal Stress on Dimorphos Material Displacement and Resurfacing Possibility

Periodic tidal stress studies done preencounter found that local material failure due to tides was only possible for a cohesionless Dimorphos with very low friction angle, i.e., 10°, and failure was restricted to surface layers at the poles for homogeneous models and at the equator for layered internal-structure models Murdoch et al. 2017a). This result, however, was made using models based on monolithic rocks, did not take into account the rotation of the satellite, and underestimated the oblateness of Dimorphos Daly et al. 2023).

From the latest DART results, considering a weaker rubble-pile model instead and matching the estimated shape and rotation of Dimorphos would increase tidal stress inside Dimorphos up to a few tenths of a pascal in amplitude. This is an order of magnitude lower than the upper bound of the best- t results with the DART observables in Raducan et al. 2024a) where cohesion is estimated to be lower than a few pascals, consistent with the results of Cheng et al. 2024) where cohesion was found to be lower than 500 Pa with no lower limit. If cohesion of $\gtrsim$0.1 Pa is present, tidal resurfacing and faults due to tidal stress are unlikely to occur at the surface of Dimorphos for synchronous rotation. Local resurfacing from nontidal effects can still happen; due to structural readjustment of the whole asteroid, slight deformation about the impact antipodal site and moderate surface refreshment are still possible Liu et al. 2023).

However, in addition to Dimorphos s excited postimpact orbital state, its rotation state could have been signi cantly excited and possibly entered tumbling; Agrusa et al. 2021). As a result, the tidal, centrifugal, and Euler accelerations felt by boulders on Dimorphos s surface can undergo signi cant orbit-to-orbit changes. This can lead to surface slope changes on the order of tens of degrees Agrusa et al. 2022b). Depending on the postimpact shape of Dimorphos i.e., the initial surface slopes), this may lead to motion on Dimorphos s surface long after the impact. However, this effect is dif cult to quantify, as it depends strongly on Dimorphos s unknown postimpact rotation state and shape. These various sources of resurfacing suggest that Dimorphos may look very different upon Hera s arrival in late 2026 than it would have immediately following impact. Distinguishing between surface features i.e., crater morphology) that were created directly by the impact from these longer-term resurfacing processes will present a unique challenge to the Hera team Section 5).

4.3.2. Large-scale Reshaping of Dimorphos

Recent impact simulations have revealed that, if Dimorphos is indeed a structurally weak, low-cohesion body, the DART impact could have caused large-scale reshaping beyond just forming an impact crater Raducan & Jutzi 2022; Raducan et al. 2022; Stickle et al. 2022; Raducan et al. 2024b). Material displacement and compaction around the impact site likely caused Dimorphos to become more elongated according to these simulations and Dimorphos s equatorial axis ratio a_s b_s could reach 1.2 Raducan et al. 2024a), a signi cant difference from its preimpact value of 1.06 ± 0.03.

Interestingly, ground-based observations also corroborate the elongated shape of the postimpact Dimorphos. While none were detected in the preimpact lightcurve data, recent high-quality lightcurve data revealed secondary lightcurve variations corresponding to Dimorphos s rotation Pravec et al. 2024). From these data, the upper bound of a_s b_s is estimated to be 1.4. Though this estimate carries some uncertainties due to the unknown attitude state of Dimorphos, it aligns well with the estimate from a recent impact simulation Raducan et al. 2024a). Additionally, postimpact orbit tting using mutual-event observations over 5 months, accounting for the planar F2BP Naidu et al. 2024), also leads to a similar a_s b_s, 1.306 ± 0.012, as well as a polar axis ratio b_s c_s of 1.2 ± 0.2 Table 2).

Considering these numerical and observational constraints, reshaping of Dimorphos appears to be highly plausible. Consequently, it is important to consider the effect of reshaping on the mutual dynamics of the Didymos system. The elongation of Dimorphos leads to a change in its orbital period Nakano et al. 2022), which is critical to account for in the β estimation process. Moreover, the postimpact shape is likely to have some degree of asymmetry, as the leading side of Dimorphos undergoes more signi cant reshaping than the opposite side. This asymmetry could influence Dimorphos s attitude dynamics and increase the likelihood of postimpact attitude instability. These effects of Dimorphos s reshaping will be discussed further in Section 4.4.

In addition, the DART impact caused a change in the shape of Dimorphos outside of a stable shape dynamical con guration that may be providing a continuous reservoir of material that maintains the tail. The resettling timescale is largely determined by the microgravity environment of the system, and thus a continuous active release of particles up through the present time cannot be ruled out. Investigation into the timescale of how Dimorphos settles into a new shape and dynamical con guration is ongoing.

4.4. Reshaping-induced Perturbations on the Mutual Dynamics

Nakano et al. 2022) conducted a preimpact statistical investigation into the effect of Dimorphos s reshaping on the mutual dynamics, speci cally focusing on the orbital period—one of the key parameters in estimating β. The current estimate of a_s $b_s \sim 1.3$, however, exceeds the range explored in the preimpact study. Here, we consider a range of a_s b_s from 1.1 to 1.5, which thoroughly encompasses the current estimates of a_s b_s with the uncertainties owing to Dimorphos s unknown attitude state and investigate the effect of signi cant reshaping on not only the orbital period but also the attitude state of Dimorphos.

Following Nakano et al. 2022), we generate synthetic shape models of Dimorphos in its reshaped form Figure 9 a)) and propagate the mutual dynamics using a nite-element F2BP model. In order to constrain speci cally the effect of reshaping, the simulations do not account for the momentum and torque imparted by the DART spacecraft and only consider Dimorphos s reshaping. We assume that Dimorphos experiences instantaneous reshaping under constant volume. Assuming that the angular momentum is conserved before and after reshaping, the angular velocity of the reshaped Dimorphos is adjusted in each simulation based on the modi ed moment of inertia due to reshaping. This ensures that the system s initial state is dynamically consistent throughout the simulations. We compute the reshaping-induced orbital-period change by comparing the orbital period of the reshaped Dimorphos with that of the nominal, preimpact state see Table 2). Dimorphos s attitude

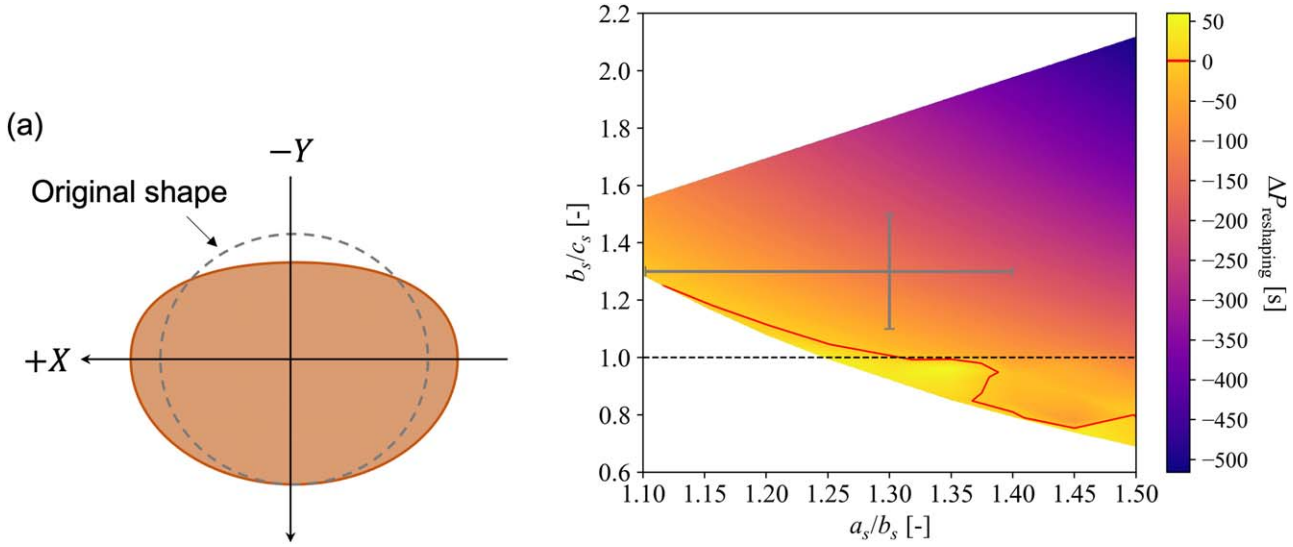

Figure 9 a) Schematic diagram showing a synthetic shape model of a reshaped Dimorphos. The axes are in Dimorphos s body- xed frame, with the *X*- and *Y*-axis corresponding to the long and intermediate axis, respectively. We consider a physically plausible reshaping condition inferred from recent impact simulations and describe such reshaping by changing the positive and negative sides of the *X*-, *Y*-, and *Z*-axis of the original Dimorphos shape model. We assume that the impact, which was approximately aligned with the *Y*-axis, instantaneously shortened the *Y*-axis and lengthened the *X*-axis. The *Z*-axis is modi ed such that the volume of Dimorphos before and after reshaping does not change. b) Reshaping-induced orbital-period change, $P_{\text{reshaping}}$, as a function of the synthetic shape model s a_s b_s and b_s c_s that are permissible under the physically plausible reshaping condition. The red curve denotes $P_{\text{reshaping}} = 0$ s. The current estimates of the axis ratios a_s b_s and b_s c_s are indicated by the horizontal and vertical error bars, respectively i.e., 1.1 a_s b_s 1.4 from Pravec et al. 2024; a_s $b_s = 1.300 \pm 0.010$ and b_s $c_s = 1.3 \pm 0.2$ from Naidu et al. 2024).

state after reshaping is described by using the 1–2–3 roll, pitch, and yaw Euler angles as used in Section 2.2.

4.4.1. Orbital-period Change and ΔV_T

Figure 9 b) shows the reshaping-induced orbital-period change, $P_{\text{reshaping}}$, as a function of the synthetic shape model s a_s b_s and b_s c_s. We nd that most of the shapes result in a reduction of the orbital period, but a subset of the shapes, characterized by b_s c_s close to or less than unity, can lead to an increase of the orbital period. The red contour line indicates $P_{\text{reshaping}} = 0$ s. The unsmooth contour below b_s $c_s < 1.0$ is because of the orbital-period variation owing to the unstable attitude of Dimorphos, as discussed in Section 2.3. In the same gure, the horizontal and vertical error bars correspond to the current estimates for a_s b_s and b_s c_s 1.1 a_s b_s 1.4 from Pravec et al. 2024; a_s $b_s = 1.300 \pm 0.010$ and b_s $c_s = 1.3 \pm 0.2$ from Naidu et al. 2024). Note that the synthetic shape models used here have symmetric con gurations about the *Y*-axis Figure 9 a)); our investigation revealed that minor asymmetries in shape do not exert any signi cant effect on $P_{\text{reshaping}}$ Nakano et al. 2024).

Should postimpact Dimorphos fall within the uncertainty range de ned by the error bars in Figure 9 b), the resulting $P_{\text{reshaping}}$ ranges from $\sim$ 250 to $\sim$+10 s. This implies that within the observed 33 minute orbital-period change, as much as $\sim$4 minutes could potentially be attributed to Dimorphos s reshaping, as opposed to being solely attributed to the momentum change caused by the DART impact and ejecta recoil.

The tangential component of Dimorphos s orbital-velocity change V_T corresponding to $P_{\text{reshaping}}$ of 250 to +10 s can be computed; it ranges from 0.347 to 0.014 mm s ^{1} Nakano et al. 2024). The initial estimate of V_T, –2.70 $\pm$ 0.10 mm s ^{1}, did not account for the effect of Dimorphos s reshaping Meyer et al. 2023b; Cheng et al. 2023). However, as the effects of reshaping and the DART impact are independent to rst order Nakano et al. 2022), adding this V_T from reshaping to the earlier estimate of V_T would lead to a good approximation of the true V_T and thus β, effectively accounting for Dimorphos s reshaping. This adjustment can be made once the postimpact Dimorphos s shape is thoroughly characterized through the Hera mission.

4.4.2. Attitude Perturbation

Reshaping of Dimorphos, particularly for the magnitude considered in this study i.e., a_s b_s from 1.1 to 1.5), generally leads to an excitement of roll and pitch angles with an amplitude of less than 10 and yaw angles with an amplitude of about 20 . However, as can be seen from Figure 10 a), shapes with b_s c_s below $\sim$1.0 could experience higher amplitudes, particularly exceeding 90 in the roll angle. These shapes also experience high amplitudes in both pitch and yaw angle, although the amplitudes remain relatively small compared to the roll direction. This is likely attributed to the asymmetric con guration about the long axis *X*-axis) caused by the impact Figure 9 a)). The leading side of Dimorphos experiences more severe reshaping than the other side, inducing a stronger tendency for the body to roll about its long axis. Despite the instability induced by Dimorphos s reshaping, the body generally remains tidally locked with Didymos.

However, it is important to recognize that the orientations of the principal axes for the synthetic shape models considered thus far roughly align with those of the preimpact Dimorphos. This alignment arises from the assumption that reshaping occurs along the original principal axes. If this is not the case, that is, if reshaping occurs along off-principal axes, Dimorphos s attitude becomes even more perturbed. We have thus conducted an additional investigation accounting for the off-principal axes reshaping of Dimorphos. The off-principal axes reshaping was parameterized with two angles, the in-plane

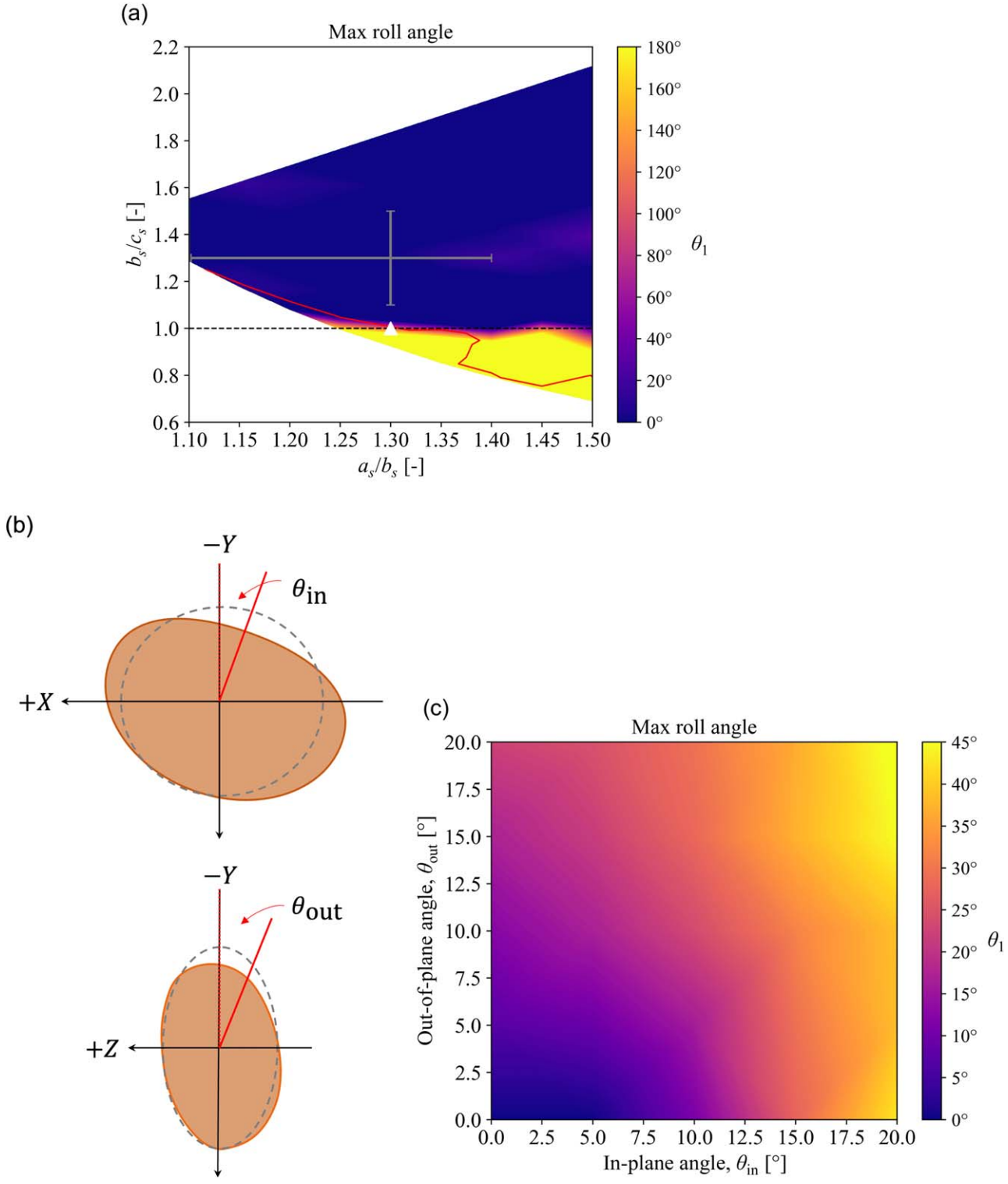

Figure 10 a) Maximum roll angle amplitude as a function of the synthetic shape model s axis ratios a_s b_s and b_s c_s. The red curve denotes $P_{\text{reshaping}} = 0$ s from Figure 9 b). The error bars denote the postimpact axis ratios and their uncertainties Table 2). b) A top and side view of a synthetic shape model of Dimorphos under off-axial reshaping. The in-plane reshaping angle θ_{in} and the out-of-plane reshaping angle θ_{out} are measured from Dimorphos s intermediate axis Y-axis). c) Maximum roll angle amplitude as a function of θ_{in} and θ_{out}.

reshaping angle, θ_{in}, and the out-of-plane reshaping angle, θ_{out}, as depicted in Figure 10 b), and the nite-element F2BP model Nakano et al. 2022) was used to simulate the attitude dynamics of Dimorphos. In Figure 10 c), we show the roll angle amplitude of a synthetic shape model with a_s $b_s = 1.3$ and b_s $c_s = 1.1$ as a function of the in-plane reshaping angle θ_{in} and the out-of-plane reshaping angle θ_{out} measured from the intermediate axis Y-axis). Notably, the attitude state can exhibit signi cant deviations from the principal-axes reshaping case i.e., $\theta_{\text{in}} = \theta_{\text{out}} = 0°$). Similar sensitivity to θ_{in} and θ_{out} is observed in the pitch and yaw angles. This result highlights the dif culty of predicting Dimorphos s attitude state without

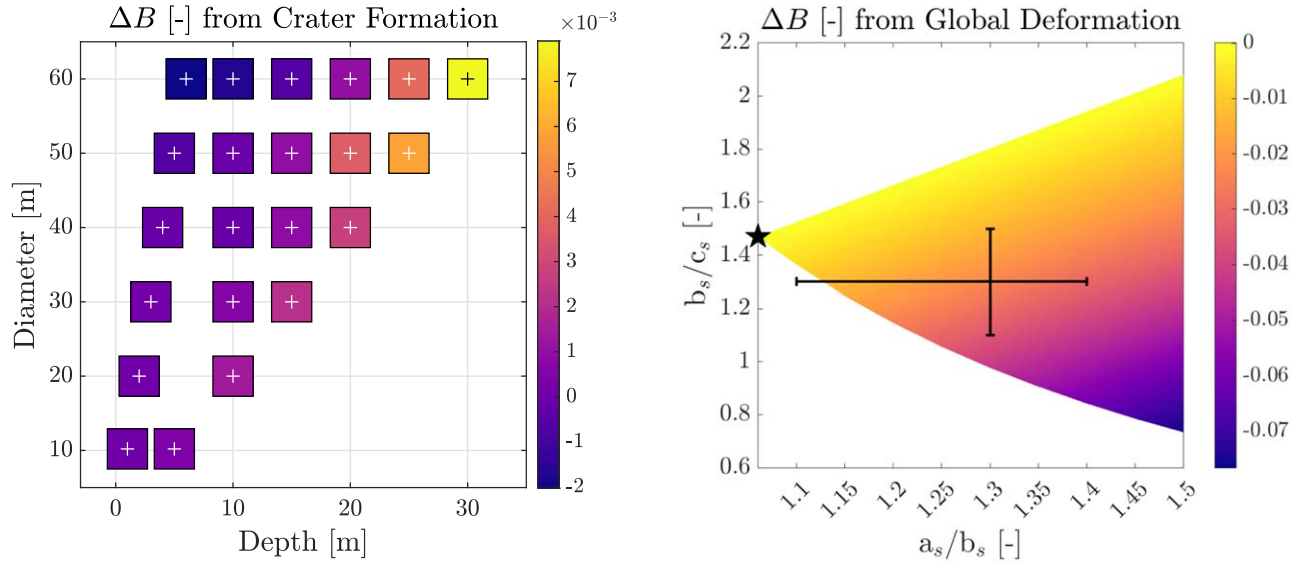

Figure 11 Changes in the BYORP coef cient, B, as a function of crater depth and diameter left) and postimpact elongation ratios a_s b_s and b_s c_s under physically plausible deformation right). The white black crosshairs in the crater plot mark the speci c depth and diameter values corresponding to each case. The colored boxes surrounding the crosshairs indicate the magnitude of B. The black error bars denote the current estimates of the axis ratios a_s b_s and b_s c_s a_s $b_s = 1.300 \pm 0.010$ and b_s $c_s = 1.3 \pm 0.2$ from Naidu et al. 2024; with the 1.1 a_s b_s 1.4 range from Pravec et al. 2024). The black star represents the preimpact elongation ratios provided in Table 2.

precise knowledge of its postimpact shape. Even if the axis ratios of the postimpact shape are constrained through numerical and observational means, the attitude state could be signi cantly different, depending on how different the orientations of the new principal axes are from the original principal axes.

Importantly, the discussed attitude instability of Dimorphos is solely a consequence of reshaping. As discussed in Section 2.2, Dimorphos s attitude instability including NPA rotation is plausible, considering the preimpact shape and β, even without reshaping. The ndings presented here suggest that Dimorphos s reshaping further increases the likelihood of such attitude instability.

4.5. Secular Evolutionary Effects

The long-term dynamical evolution of rubble-pile binary asteroid systems is driven by BYORP and tides. A full discussion on these phenomena and how they affect binary asteroid evolution can be found in Richardson et al. 2022). Note that the BYORP effect is dependent on the shape of the secondary, from which a set of Fourier coef cients can be computed McMahon & Scheeres 2010). These coef cients are based solely on the shape model of the secondary asteroid. The dominant along-track coef cient, denoted B, is the indicator for the direction of evolution. A positive B corresponds to expansive BYORP, while a negative B corresponds to contractive BYORP. Prior to DART, little was known about the BYORP coef cient or tidal parameters of Dimorphos. It is still dif cult to constrain these quantities, but work has been done in Cueva et al. 2024) to bound predictions of how much B could have changed from the DART impact, and the resulting implications for the dynamical evolution.

We assume a preimpact shape of a smooth oblate spheroid with nominal extents along the x, y, z) axes of 179, 169, and 115 m, respectively, from Daly et al. 2024; corresponding to a near-zero BYORP coef cient) and tidal–BYORP equilibrium, as Didymos is suspected to be at or close to this state Richardson et al. 2022; Scheirich & Pravec 2022; Scheirich et al. 2024). A nominal B was computed for the assumed preimpact shape model following the methodology in Scheeres 2007). We explore two avenues of reshaping, cratering and global deformation, and evaluate the shape s effect on B. This is done by modifying the preimpact shape model and recomputing B to quantify how much B deviates from the nominal value. For the rst regime, craters of various depths and diameters are placed at the estimated impact location of 8.°84 ± 0.°45 S, 264.°30 ± 0.°47 E Daly et al. 2023). For global deformation, we use the methodology described in Nakano et al. 2022) and used in Section 4.4 to explore deformed shapes ranging from a_s $b_s = 1.06$ to 1.5. We nd that craters in general lead to a net positive change in B, but a large, shallow crater can cause a net negative change. All global deformation cases resulted in a net negative change in B since flattening occurred on the leading hemisphere of Dimorphos. The change in magnitude becomes larger with more elongated secondaries and or flatter deformed leading hemispheres. The change in B for the nominal postimpact elongations of a_s $b_s = 1.3$ and b_s $c_s = 1.3$ Table 2) is $B = 2.33 \times 10^{-2}$. These elongation values are from the nal orbital solution used throughout this paper Naidu et al. 2024), therefore this is the latest estimation of B for Dimorphos and is an update from the original value reported in Cueva et al. 2024). For reference, the preimpact B value for Dimorphos is expected to be on the order of 5×10^{-3}, depending on the true strength of tides Cueva et al. 2024). The change in magnitude of B for both craters and global deformation are shown in Figure 11.

We ran dynamical simulations of the attitude and mutual orbit dynamics incorporating forces and torques from solar-radiation pressure, tidal dissipation on both the primary and secondary, and solar third-body effects. The binary system s heliocentric orbit was also modeled in the simulations, which has a semimajor axis of 1.64 au, eccentricity of 0.38, and inclination of 3.°4 with respect to the ecliptic Richardson et al. 2022). The B values for both cratering and global

deformation were added to three theoretical equilibrium B values corresponding to three different tidal strengths. Cases were run for 10,000 simulated years in order to assess the initial result of the impact on the attitude of the secondary, as well as the long-term behavior of the system. Simulation results of the orbit and attitude evolution of Dimorphos are presented in Cueva et al. 2024). Trends and observations from these results are summarized here. We nd that the BYORP coef cient increases but remains negative for most crater cases, thus driving the semimajor axis to a new higher) theoretical equilibrium orbital radius. Planar libration is excited for these cases. Large, deep crater morphologies can cause the true value of B to become positive depending on the tidal strength), resulting in joint expansive evolution with a theoretically unbounded semimajor axis. This ties in with the overall life cycle of rubble-pile binaries. Although expansive BYORP means it will work with tides to grow the orbit, there are a lot of factors that could affect the subsequent evolution and end state of the system. For example, Dimorphos could lose synchronicity with weakening tides from the expansion, stopping the evolution. This could result in a wide asynchronous binary system Jacobson et al. 2014). Another possibility is that Dimorphos could escape the Hill radius of the orbit and form an asteroid pair, where the two bodies share a similar heliocentric orbit but are no longer bounded by a mutual orbit Jacobson & Scheeres 2011). Due to the chaotic nature of the dynamics, it is dif cult to predict exactly what would happen if the DART impact caused expansive BYORP.

As for the global deformation cases, we found that the system can experience a wide range of evolutionary behavior depending on the magnitude of reshaping and thus magnitude of inertial changes), tidal strength, and initial conditions. We observed cases with excitation of planar librations, tumbling, and barrel instability. Some cases with planar libration had a quick onset of nonplanar libration, likely due to resonances with the heliocentric orbit. Some cases recaptured in the 1:1 spin–orbit resonance, while some remained chaotic for the entire 10,000 yr simulation run. For cases that experience synchronous recapture after a period of chaos, we saw that the secondary can either recapture in its original orientation, or a different orientation where it has flipped 180 about its minor axis, flipped 180 about its major axis, or both—thus possibly leading to orbital expansion.

The range of results from Cueva et al. 2024) show that until the true postimpact spin state and shape of Dimorphos are resolved by Hera, it is dif cult to assert exactly how the system s secular evolution changed from the impact. The detection of BYORP from Hera is unlikely due to the short time span between Hera and DART, but not impossible. BYORP will still act on the system if libration is excited, but tumbling or barrel instability will shut off BYORP, and thus BYORP cannot be measured. If Hera observes that the secondary remained synchronous following the impact, then any measured drift in the orbit would be due to BYORP and tides. If Dimorphos is librating, then it gets more complicated. For example, the range of secular drift rates surrounding the nominal a_s b_s and b_s c_s is approximately 1.8 to 4.6 cm yr ^{1} corresponding to mean motion rates, $\dot{n}$, ranging from 5.5×10^{17} to 1.4×10^{16} rad s ^{2}). This equates to an inward drift of about 9–23 cm in the 5 yr gap between DART and Hera. These numbers are assuming only libration is excited from the impact. If Dimorphos is dynamically excited, which Hera will measure, there will be inevitable variations in the separation distance due to inherent orbit–attitude coupling. In the short time span between DART and Hera, it will be dif cult to distinguish any secular drift in these variations since the expected secular drift in that time span is so small. However, Hera will be able to provide a full detailed shape model of postimpact Dimorphos. While DART supplied a high-resolution shape model, it is only one side of Dimorphos, so we are unable to fully compute a B value for Dimorphos. Knowing the backside topography of Dimorphos would allow us to better resolve the preimpact shape model of Dimorphos and use its B value to constrain tidal strengths of Dimorphos from the preimpact tidal–BYORP equilibrium. The detailed postimpact shape model will allow us to re ne our predictions for how the secular evolution of the Didymos system will proceed. Knowing the B of the postimpact shape model acquired from Hera will also help us improve our computations for how much we would have expected the orbit to drift due to BYORP if the system is dynamically excited. If it in theory should drift more than we originally predicted, then it may be easier to detect BYORP.

5 Implications for Hera

The Hera spacecraft will arrive at Didymos in 2026 October and will begin in 2026 December approximately 6 months of proximity operations. Details regarding mission objectives, pro le, scenario, instrumentation, and measurements can be found in Michel et al. 2022). The primary goal of Hera is to measure the mass of Dimorphos, which is the missing parameter for the precise estimate of β, accounting for the fact that the "eventual" β is slightly higher than the "immediate" β see Section 3.3.3). This knowledge will be acquired through a series of measurements. Optical images will mainly be used to constrain the shape and dynamical state, and provide an early mass estimate during the distant flybys. Once Hera gets closer, its Radio Science Experiment RSE), involving the main spacecraft and the two CubeSats, Juventas and Milani Ferrari et al. 2021a; Gramigna et al. 2024), should obtain Dimorphos s mass to higher precision and measure the extended gravity elds and rotational states of both Didymos and Dimorphos. In this way, the RSE will also better constrain the interior structure and global properties e.g., density and porosity). The low-frequency radar called JuRa and the gravimeter called GRASS on board the Juventas CubeSat will further characterize the interior. Additionally, Hera will also enable the accurate determination of the heliocentric β by reconstructing the Didymos system ephemerides using pseudorange points Section 3.2).

Hera includes an intersatellite link ISL) transceiver for ensuring correct communication with the CubeSats, relaying their data and commands to and from the operation centers on the ground. A dedicated radio-science mode of the ISL will also allow for collecting high-precision range and range-rate measurements, which will be used in combination with Earth-based radio tracking and optical navigation images provided by the Asteroid Framing Camera AFC) on board Hera. Of particular importance are the ISL observables collected by Juventas and Milani, which orbit the system at closer distances than Hera Ferrari et al. 2021b), and allows for obtaining higher accuracies in the parameters of interest. The AFC observations will also determine the rotational states of the asteroids by tracking their surface features landmarks) and provide the necessary data to contribute to the mass measurement.

A covariance analysis has been performed to obtain the expected uncertainties in the scienti c parameters of interest for the Hera RSE. The expected formal 1 uncertainties for the *GM* of Didymos and Dimorphos are on the order of 0.01 and 0.1 , respectively. Additionally, the extended gravity elds of Didymos and Dimorphos can be estimated up to degree three and two, with a J_2 accuracy of better than 0.1 and 10 , respectively. Regarding Didymos, such measurements will offer the possibility of detecting internal heterogeneity, with implications for understanding the structural behavior of the asteroid at fast spin and the formation of Dimorphos Section 4.1.2).

Of utmost importance is getting an accurate estimate of the orbital parameters of Dimorphos, as well as its librations, since they are directly linked to the energy dissipation of the system and to the preimpact state Meyer et al. 2023a, 2023b). Measurements of those parameters may allow determination of secular effects, such as a possible orbital drift that can be linked to BYORP and tides, depending on Dimorphos s actual rotational state Section 4.5). The RSE covariance analysis indicates that Dimorphos s relative position can be retrieved with submeter-level accuracy throughout the mission, while the semimajor axis and eccentricity uncertainties are on the order of 10 ^{1} m and 10 ^{4}, respectively. Similarly, Dimorphos s spin pole can be constrained to less than 1 , while its librations can be estimated with a relative accuracy of roughly 2 $\times$ 10 ^{2} for the libration amplitude, 8×10^{4} deg h ^{1} for the angular velocity, and 2 for the phase. Note that a small perturbation in the rotational dynamics with respect to the equilibrium condition was assumed. If this is not the case, more analysis should be performed, and the results could vary.) All the details and results of the analysis can be found in Gramigna et al. 2024).

In addition, the LIDAR on board Hera, called Planetary ALTimeter, will perform range measurements that will yield independent shape reconstructions with respect to the ones provided by the AFC images and will be used to help determine the wobble of the binary system, which will yield an independent estimate of the mass of Dimorphos. These altimetric measurements could also allow for a more precise reconstruction of Hera s trajectory, enhancing the RSE scienti c return. Overall, when adding LIDAR altimetry crossover measurements, the expected improvement of Dimorphos s relative orbit is on the order of 60 for the radial and tangential components, and up to 40 for the orbit-normal one Gramigna et al. 2023).

The current questions regarding a possible shape change of Dimorphos Section 4.3.2), the actual β value, and rotational properties will thus be answered by Hera thanks to a rendezvous with the binary system and its investigation at close proximity. Regarding surface changes on Dimorphos resulting directly from the DART impact, the analysis will have to account for the long-term resurfacing processes that may contribute to the surface features i.e., crater morphology) that Hera will observe Section 4.3.1).

JuRa on board the Juventas CubeSat will reveal whether Dimorphos is a rubble pile made of boulders homogeneously distributed throughout, whether its interior contains a high level of heterogeneities, or whether it is simply made of a big core surrounded by a layer of pebbles and gravels. This has implications for binary-formation models and our interpretation of the response of the asteroid to the DART impact and to tidal forces. In turn, the possible presence of long-lived ejecta and the possibility that Dimorphos is tumbling have some implications for the operations of Hera and its two CubeSats, which need to be assessed. Operations for the Hera spacecraft that allow observing the entire surface of the asteroid may have to be adapted to this situation, as may the operations of the CubeSats that will come closer to the asteroid to perform their measurements. Furthermore, both CubeSats are expected to land on the smaller body. In particular, Juventas is planned to land on Dimorphos to perform additional measurements of the gravity eld with its gravimeter, which requires that it remains stable on the surface. Landing on a tumbling asteroid increases the complexity of the operation and has never been attempted. Nevertheless, knowing in advance that the Hera mission may face such a situation is extremely useful to be best prepared for a more complex situation than originally expected. This is now taken into account in the development of operation plans at Didymos and Dimorphos.

The Hera data will also provide opportunities to constrain the material properties of both Dimorphos and Didymos, thus feeding into the models discussed in this paper. The dynamics of the CubeSat landings on Dimorphos will be recorded with onboard accelerometers leading to direct measurements of the surface mechanical properties Murdoch et al. 2022; Sunday et al. 2022). The geology of the asteroids and the boulder morphology as observed with the Hera AFC or the CubeSat cameras can be used to constrain the mechanical properties such as the angle of internal friction Barnouin et al. 2024; Robin et al. 2024). High-resolution images of the surface of Didymos taken with different viewing and illumination geometries will constrain the currently unknown depth of the boulder tracks, allowing for an improved estimate of the bearing capacity of the surface of Didymos Bigot et al. 2024). Morphological mapping using, for example, surface-roughness measurements Vincent et al. 2024) of the asteroid pair before and after the DART impact will highlight changes due to reimpacting ejecta, resurfacing, and mass-wasting events. The penetration depth of ejecta boulders that have reimpacted the surface of Didymos at low speed will provide additional constraints on the properties of the surface material friction, density, etc.; Sunday et al. 2022).

In conclusion, Hera s mission will provide very accurate characterization of various dynamical aspects of the Didymos system, including its gravity eld, orbits, dynamics, energy dissipation processes, surface, and interior structure. Thanks to the expected level of accuracy provided by the Hera mission to determine Dimorphos s important dynamical attributes e.g., mass, rotational state, and orbit), a more re ned value of β can be estimated, which in turn will signi cantly increase the understanding and validation of the kinetic impactor technique for deflecting potentially hazardous asteroids in the future.

6 Conclusions

Following the successful demonstration of kinetic impact provided by the DART mission, the dynamical state of the Didymos system before and after the event was assessed. The main conclusions are as follows.

1. The postimpact eccentricity is consistent with a circular preimpact orbit and the postimpact precession rate strongly suggests impact-induced reshaping of

Dimorphos. The possibility of an unstable rotation state of Dimorphos should be investigated further.

2. The DART impact momentum transfer enhancement factor β was found to be about 3.6 assuming a nominal bulk density of 2400 kg m ^{3} for Dimorphos. Although some dynamical parameters have been revised since that determination, the uncertainty in β remains dominated by the large uncertainty in the mass of Dimorphos. It is still too early for a heliocentric β measurement, but future occultations and Hera s arrival should give strong constraints. It is evident that the impact generated a lot of ejecta $\sim 10^{7}$ kg), despite the likely mitigating effect of target surface curvature. A possible secular decrease in orbital period in the days following impact may be evidence of coupling between the binary and persistent ejecta.
3. Didymos s rapid spin, oblate shape, and comparatively high bulk density suggest global cohesion may not be required to maintain its structural stability at present. Given its shape and the likely formation of Dimorphos from the accumulation of material shed by its parent, Didymos probably has an internal structure of moderate strength. High-slope surface features and the lack of any detectable spin change suggest a surface cohesion of a few pascals, consistent with granular impact simulations. The unexpected oblate shape of Dimorphos implies a more complex formation pathway than simply accretion at the Roche limit. Impact simulations suggest Dimorphos may have reshaped signi cantly, a possibility borne out by preliminary lightcurve measurements and dynamical modeling indicating a postimpact elongated shape. This in turn may have contributed to some of the measured β and increases the probability of Dimorphos being in a tumbling state. All of these considerations are important for the long-term secular evolution of the system due to tides and BYORP, with a range of possible outcomes that will likely require Hera to resolve.
4. Hera will greatly reduce the uncertainties on Dimorphos s mass and therefore on β, as well as on Dimorphos s shape, rotation state, and internal properties thanks to a wide array of measurement instruments. The possibly tumbling Dimorphos has some implications for the operation of Hera and its two CubeSats that need to be assessed and are being taken into account in the development of operation plans.

The DART mission, together with the Didymos observing campaign, not only represented the rst test at realistic scale of a hazard mitigation technique but also provided unprecedented measurements of dynamical effects in a nonideal small solar system binary for testing theoretical models. Predictions prior to encounter were largely borne out, but there were some surprises and there remain unanswered questions. We look forward to revelations from the Hera mission, which promise to further re ne our understanding of small bodies in general and the formation and evolution of binary asteroids in particular.

Acknowledgments

We thank Paula Benavidez, Özgür Karatekin, and the anonymous reviewers who provided comments that helped improve this paper.

The work presented here was supported in part by the DART mission, NASA Contract 80MSFC20D0004 to JHU APL. Part of this work was supported by the Programme National de Planétologie PNP) of CNRS-INSU cofunded by CNES, by CNES itself, and by the BQR program of the Observatoire de la Côte d Azur. The ACROSS project is supported under the OSIP ESA CONTRACT No. 4000135299 21 NL GLC ov. This study makes use of data obtained by the Observing Working Group of the DART Investigation Team. Some simulations were performed on the ASTRA cluster administered by the Center for Theory and Computation, part of the Department of Astronomy at the University of Maryland.

H.F.A. was supported by the French government, through the UCA J.E.D.I. Investments in the Future project managed by the National Research Agency ANR) with the reference number ANR-15-IDEX-01. R.H.C. acknowledges that this material is based upon work supported by the National Science Foundation Graduate Research Fellowship Program under grant No. DGE 2040434. Any opinions, ndings, and conclusions or recommendations expressed in this material are those of the author s) and do not necessarily reflect the views of the National Science Foundation. F.F. acknowledges funding from the European Research Council ERC) under the European Union s Horizon Europe research and innovation program grant agreement No. 101077758). R.M. acknowledges that this work was supported by a NASA Space Technology Graduate Research Opportunities NSTGRO) award, NASA contract No. 80NSSC22K1173. P.M. acknowledges support from the French space agency CNES and ESA. R.N. acknowledges support from NASA FINESST NNH20ZDA001N). Y.Z. acknowledges the support provided by NASA through grant HST-GO-17292 from the Space Telescope Science Institute, which is operated by the Association of Universities for Research in Astronomy, under NASA contract NAS 5-26555.

A.C.B., E.G., M.J., P.M., R.L.M., S.D.R., P.T., K.T., and M. Z. acknowledge funding support from the European Union s Horizon 2020 research and innovation program under grant agreement No. 870377 project NEO-MAPP). The work of S. R.C, E.G.F, and S.P.N was carried out at the Jet Propulsion Laboratory, California Institute of Technology, under a contract with the National Aeronautics and Space Administration 80NM0018D0004). E.G., R.L.M., M.Z., and P.T. wish to acknowledge Caltech and the NASA Jet Propulsion Laboratory for granting the University of Bologna a license to an executable version of MONTE Project Edition S W. E. G., R.L.M., A.R., M.Z., and P.T. are grateful to the Italian Space Agency ASI) for nancial support through Agreement No. 2022-8-HH.0 in the context of ESA s Hera mission. M.J. and S.D.R. acknowledge support by the Swiss National Science Foundation project number 200021 207359). J.M. acknowledges support from the DART Participating Scientist Program 80NSSC21K1048). F.M. acknowledges nancial support from grants PID2021123370OB-I00 and CEX2021-001131-S funded by MCIN AEI 10.13039 501100011033. N.M. acknowledges funding support from the European Commission s Horizon 2020 research and innovation program under grant agreement No. 870377 NEO-MAPP project) and support from the Centre National d Etudes Spatiales CNES), focused on the Hera space mission. L.P. was supported by an appointment to the NASA Postdoctoral Program at the NASA Jet Propulsion Laboratory, California Institute of Technology, administered by Oak Ridge Associated Universities under

contract with NASA. P.P. and P.S. acknowledge support by the Grant Agency of the Czech Republic, grant 23-04946S. S.R.S. acknowledges support from the DART Participating Scientist Program, grant no. 80NSSC22K0318. D.S. acknowledges support of the France-USA Fulbright Commission while a Fulbright Visiting Scholar 2022–2023) at UC Berkeley and thanks Action Fédératrice Gaia of the Paris Observatory for nancial support. G.T. acknowledges nancial support from project FCE-1-2019-1-156451 of the Agencia Nacional de Investigación e Innovación ANII and Grupos I+D 2022 CSIC-Udelar Uruguay). P.T., A.R., and M.Z. acknowledge nancial support from Agenzia Spaziale Italiana ASI, contract No. 2019-31-HH.0 CUP F84I190012600). J.M.T.-R. acknowledges support from the Spanish project PID2021-128062NB-I00 funded by MCIN AEI.

ORCID iDs

Derek C. Richardson https: orcid.org 0000-0002-0054-6850
Harrison F. Agrusa https: orcid.org 0000-0002-3544-298X
Brent Barbee https: orcid.org 0000-0003-3739-3242
Rachel H. Cueva https: orcid.org 0009-0000-2266-6266
Fabio Ferrari https: orcid.org 0000-0001-7537-4996
Seth A. Jacobson https: orcid.org 0000-0002-4952-9007
Rahil Makadia https: orcid.org 0000-0001-9265-2230
Alex J. Meyer https: orcid.org 0000-0001-8437-1076
Patrick Michel https: orcid.org 0000-0002-0884-1993
Ryota Nakano https: orcid.org 0000-0002-9840-2416
Yun Zhang https: orcid.org 0000-0003-4045-9046
Paul Abell https: orcid.org 0000-0002-6233-1820
Colby C. Merrill https: orcid.org 0000-0002-5566-0618
Adriano Campo Bagatin https: orcid.org 0000-0001-9840-2216
Olivier Barnouin https: orcid.org 0000-0002-3578-7750
Nancy L. Chabot https: orcid.org 0000-0001-8628-3176
Andrew F. Cheng https: orcid.org 0000-0001-5375-4250
Steven R. Chesley https: orcid.org 0000-0003-3240-6497
R. Terik Daly https: orcid.org 0000-0002-1320-2985
Siegfried Eggl https: orcid.org 0000-0002-1398-6302
Carolyn M. Ernst https: orcid.org 0000-0002-9434-7886
Eugene G. Fahnestock https: orcid.org 0000-0003-1391-5851
Tony L. Farnham https: orcid.org 0000-0002-4767-9861
Oscar Fuentes-Muñoz https: orcid.org 0000-0001-5875-1083
Edoardo Gramigna https: orcid.org 0000-0001-8776-7922
Douglas P. Hamilton https: orcid.org 0000-0002-5010-0574
Masatoshi Hirabayashi https: orcid.org 0000-0002-1821-5689
Martin Jutzi https: orcid.org 0000-0002-1800-2974
Josh Lyzhoft https: orcid.org 0000-0001-6420-8423
Riccardo Lasagni Manghi https: orcid.org 0000-0002-5733-2554
Jay McMahon https: orcid.org 0000-0002-1847-4795
Fernando Moreno https: orcid.org 0000-0003-0670-356X
Naomi Murdoch https: orcid.org 0000-0002-9701-4075
Shantanu P. Naidu https: orcid.org 0000-0003-4439-7014
Eric E. Palmer https: orcid.org 0000-0001-6755-8736
Paolo Panicucci https: orcid.org 0000-0003-3743-6302
Laurent Pou https: orcid.org 0000-0001-9619-7271
Petr Pravec https: orcid.org 0000-0001-8434-9776
Sabina D. Raducan https: orcid.org 0000-0002-7478-0148
Andrew S. Rivkin https: orcid.org 0000-0002-9939-9976
Alessandro Rossi https: orcid.org 0000-0001-9311-2869
Paul Sánchez https: orcid.org 0000-0003-3610-5480
Daniel J. Scheeres https: orcid.org 0000-0003-0558-3842
Peter Scheirich https: orcid.org 0000-0001-8518-9532
Stephen R. Schwartz https: orcid.org 0000-0001-5475-9379
Damya Souami https: orcid.org 0000-0003-4058-0815
Gonzalo Tancredi https: orcid.org 0000-0002-4943-8623
Paolo Tanga https: orcid.org 0000-0002-2718-997X
Paolo Tortora https: orcid.org 0000-0001-9259-7673
Josep M. Trigo-Rodríguez https: orcid.org 0000-0001-8417-702X
Kleomenis Tsiganis https: orcid.org 0000-0003-3334-6190
John Wimarsson https: orcid.org 0009-0004-6736-309X
Marco Zannoni https: orcid.org 0000-0002-4151-9656

References

Abe, S., Mukai, T., Hirata, N., et al. 2006, Sci, 312, 1344
Agrusa, H. F., Ballouz, R., Meyer, A. J., et al. 2022b, A&A, 664, L3
Agrusa, H. F., Ferrari, F., Zhang, Y., Richardson, D. C., & Michel, P. 2022a, PSJ, 3, 158
Agrusa, H. F., Gkolias, I., Tsiganis, K., et al. 2021, Icar, 370, 114624
Agrusa, H. F., Zhang, Y., Richardson, D. C., et al. 2024, PSJ, 5, 54
Ai, J., Chen, J.-F., Rotter, J. M., & Ooi, J. Y. 2011, Powder Technology, 206, 269
Ballouz, R.-L., Walsh, K. J., Sánchez, P., et al. 2021, MNRAS, 507, 5087
Barnouin, O., Ballouz, R.-L., Marchi, S., et al. 2024, NatCo, 15, 6202
Barnouin, O. S., et al. 2019, NatGe, 12, 247
Becker, T. M., Howell, E. S., Nolan, M. C., et al. 2015, Icar, 248, 499
Belton, M. J. S., Chapman, C. R., Thomas, P. C., et al. 1995, Natur, 374, 785
Bigot, J., Lombardo, L., Murdoch, N., et al. 2024, NatCo, 15, 6204
Campo Bagatin, A., Dell Oro, A., Benavidez, P. G., et al. 2023, LPICo, 2851, 2168
Chabot, N. L., Rivkin, A. S., Cheng, A. F., et al. 2024, PSJ, 5, 49
Cheng, A. F., Agrusa, H. F., Barbee, B. W., et al. 2023, Natur, 616, 457
Cheng, A. F., Raducan, S. D., Fahnestock, E. G., et al. 2022, PSJ, 3, 131
Cheng, A. F., Raducan, S. D., Jutzi, M., et al. 2024, PSJ, 5, 118
Cheng, A. F., Stickle, A. M., Fahnestock, E. G., et al. 2020, Icar, 352, 113989
Cueva, R. H., McMahon, J. W., Meyer, A. J., et al. 2024, PSJ, 5, 48
Ćuk, M., & Nesvorný, D. 2010, Icar, 207, 732
Daly, R. T., Ernst, C. M., Barnouin, O. S., et al. 2023, Natur, 616, 443
Daly, R. T., Ernst, C. M., Barnouin, O. S., et al. 2024, PSJ, 5, 24
Davis, A. B., & Scheeres, D. J. 2020, Icar, 341, 113439
Davis, A. B., & Scheeres, D. J., 2021 GUBAS: General Use Binary Asteroid Simulator, Astrophysics Source Code Library, ascl:2107.013
Deshapriya, J. D. P., Hasselmann, P. H., Gai, I., et al. 2023, PSJ, 4, 231
Dotto, E., Deshapriya, J., Gai, I., et al. 2024, Natur, 627, 505
Fahnestock, E. G., Cheng, A. F., Ivanovski, S., et al. 2022, PSJ, 3, 206
Ferrari, F., Franzese, V., Pugliatti, M., Giordano, C., & Topputo, F. 2021a, AdSpR, 67, 2010
Ferrari, F., Franzese, V., Pugliatti, M., Giordano, C., & Topputo, F. 2021b, JAnSc, 68, 973
Ferrari, F., Raducan, S. D., Soldini, S., & Jutzi, M. 2022, PSJ, 3, 177
Ferrari, F., & Tanga, P. 2022, Icar, 378, 114914
Ferrari, F., Panicucci, P., Merisio, G., et al. 2024, NatCo, submitted
Ferreira, J. F., Tanga, P., Spoto, F., Machado, P., & Herald, D. 2022, A&A, 658, A73
Gramigna, E., Lasagni Manghi, R., Zannoni, M., et al. 2024, P&SS, 246, 105906
Gramigna, E., Manghi, R. L., Zannoni, M., et al. 2023, EGU23, the 25th EGU General Assembly, EGU23–9586
Graykowski, A., Lambert, R. A., Marchis, F., et al. 2023, Natur, 616, 461
Hirabayashi, M., Raducan, S.D., Sunshine, J.M., Farnham, T.L., et al. 2024, NatCo, submitted
Gudebski, T., Heldridge, E., McGawn, B., et al. 2023, RNAAS, 7, 178
Hirabayashi, M., Ferrari, F., Jutzi, M., et al. 2022, PSJ, 3, 140
Hirabayashi, M., Sánchez, D. P., & Scheeres, D. J. 2015, ApJ, 808, 63
Holsapple, K. A. 2022, P&SS, 219, 105529
Holsapple, K. A., & Michel, P. 2006, Icar, 183, 331
Jacobson, S. A., & Scheeres, D. J. 2011, Icar, 214, 161
Jacobson, S. A., Scheeres, D. J., & McMahon, J. 2014, ApJ, 780, 60
Jewitt, D., Kim, Y., Li, J., & Mutchler, M. 2023, ApJL, 952, L12

Kareta, T., Thomas, C., Li, J.-Y., et al. 2023, ApJL, 959, L12
Kim, Y., & Jewitt, D. 2023, ApJL, 956, L26
Li, J.-Y., Hirabayashi, M., Farnham, T. L., et al. 2023, Natur, 616, 452
Liu, P. Y., Campo-Bagatin, A., Benavidez, P. G., & Richardson, D. C. 2023, MNRAS, 532, 1129
Madeira, G., Charnoz, S., & Hyodo, R. 2023, Icar, 394, 115428
Makadia, R., Chesley, S. R., Farnocchia, D., et al. 2024, PSJ, 5, 38
Makadia, R., Raducan, S. D., Fahnestock, E. G., & Eggl, S. 2022, PSJ, 3, 184
McMahon, J., & Scheeres, D. 2010, CeMDA, 106, 261
Meyer, A. J., Agrusa, H. F., Richardson, D. C., et al. 2023b, PSJ, 4, 141
Meyer, A. J., Gkolias, I., Gaitanas, M., et al. 2021, PSJ, 2, 242
Meyer, A. J., Scheeres, D. J., Agrusa, H. F., et al. 2023a, Icar, 391, 115323
Michel, P., Küppers, M., Bagatin, A. C., et al. 2022, PSJ, 3, 160
Moreno, F., Bagatin, A. C., Tancredi, G., et al. 2023, PSJ, 4, 138
Moreno, F., Campo Bagatin, A., Tancredi, G., Liu, P.-Y., & Domínguez, B. 2022, MNRAS, 515, 2178
Murdoch, N., Duchêne, A., Segovia-Otera, J., et al. 2022, EPSC, 16, EPSC2022–910
Murdoch, N., Hempel, S., Pou, L., et al. 2017a, P&SS, 144, 89
Murdoch, N., Martinez, I. A., Sunday, C., et al. 2017b, MNRAS, 468, 1259
Murray, C. D., & Dermott, S. F. 2000, Solar System Dynamics Cambridge: Cambridge Univ. Press)
Naidu, S. P., Benner, L. A. M., Brozovic, M., et al. 2020, Icar, 348, 113777
Naidu, S. P., Chesley, S. R., Farnocchia, D., et al. 2022, PSJ, 3, 234
Naidu, S. P., Chesley, S. R., Moskovitz, N., et al. 2024, PSJ, 5, 74
Naidu, S. P., Margot, J. L., Taylor, P. A., et al. 2015, AJ, 150, 54
Nakano, R., Hirabayashi, M., Agrusa, H. F., et al. 2022, PSJ, 3, 148
Nakano, R., Hirabayashi, M., Raducan, S. D., et al. 2024, PSJ, 5, 133
Nesvorný, D., Alvarellos, J. L. A., Dones, L., & Levison, H. F. 2003, AJ, 126, 398
Govender, N., & Pizette, P. 2021, in EPJ Web of Conf. 249, 9th Int. Conf. on Micromechanics on Granular Media Les Ulis: EDP Sciences), 06013
Ostro, S. J., et al. 2006, Sci, 314, 1276
Pravec, P., Fatka, P., Vokrouhlický, D., et al. 2019, Icar, 333, 429
Pravec, P., Meyer, A., Scheirich, P., et al. 2024, Icar, 418, 116138
Pravec, P., Scheirich, P., Ku nirák, P., et al. 2016, Icar, 267, 267
Pravec, P., et al. 2006, Icar, 181, 63
Radjai, F. 2018, CRMec, 346, 263
Raducan, S., Jutzi, M., Cheng, A., et al. 2024a, NatAs, 8, 445
Raducan, S. D., & Jutzi, M. 2022, PSJ, 3, 128
Raducan, S. D., Jutzi, M., Merrill, C. C., et al. 2024b, PSJ, 5, 79
Raducan, S.-D., Jutzi, M., Zhang, Y., Ormö, J., & Michel, P. 2022, A&A, 665, L10
Richardson, D. C., Agrusa, H. F., Barbee, B., et al. 2022, PSJ, 3, 157
Rivkin, A. S., Chabot, N. L., Stickle, A. M., et al. 2021, PSJ, 2, 173
Robin, C., Duchene, A., Murdoch, N., et al. 2024, NatCo, 15, 6203
Rossi, A., Marzari, F., Brucato, J. R., et al. 2022, PSJ, 3, 118
Roth, N. X., Milam, S. N., Remijan, A. J., et al. 2023, PSJ, 4, 206
Sánchez, P., & Scheeres, D. J. 2011, ApJ, 727, 120
Sánchez, P., & Scheeres, D. J. 2016, Icar, 271, 453
Sánchez, P., & Scheeres, D. J. 2018, P&SS, 157, 39
Sánchez, P., Scheeres, D. J., & Quillen, A. C. 2022, PSJ, 3, 245
Scheeres, D. J. 2007, Icar, 188, 430
Scheirich, P., & Pravec, P. 2009, Icar, 200, 531
Scheirich, P., & Pravec, P. 2022, PSJ, 3, 163
Scheirich, P., Pravec, P., Meyer, A. J., et al. 2024, PSJ, 5, 17
Schwartz, S. R., Richardson, D. C., & Michel, P. 2012, Granular Matter, 14, 363
Sharma, I. 2009, Icar, 200, 636
Souami, D., Paolo, T., Tsiganis, K., & Ferreira, J. 2022, AGUFM, NH12C–0299
Stewart, G. R., Lin, D. N. C., & Bodenheimer, P. 1984, in Planetary Rings, ed. R. Greenberg & A. Brahic Tucson, AZ: Univ. Arizona Press), 447
Stickle, A. M., DeCoster, M. E., Burger, C., et al. 2022, PSJ, 3, 248
Sunday, C., Murdoch, N., Wilhelm, A., et al. 2022, A&A, 658, A118
Tancredi, G., Liu, P.-Y., Campo-Bagatin, A., Moreno, F., & Domínguez, B. 2023, MNRAS, 522, 2403
Thomas, C. A., Naidu, S. P., Scheirich, P., et al. 2023, Natur, 616, 448
Vincent, J., Asphaug, E., Barnouin, O., et al. 2024, PSJ, submitted arXiv:2405.19764)
Vokrouhlický, D., Bottke, W. F., Chesley, S. R., Scheeres, D. J., & Statler, T. S. 2015, in Asteroids IV, ed. P Michel, F. E. DeMeo, & W. F. Bottke Tucson, AZ: Univ. Arizona Press), 509
Walsh, K. J., Ballouz, R.-L., Jawin, E. R., et al. 2022, SciA, 8, eabm6229
Walsh, K. J., & Jacobson, S. A. 2015, in Asteroids IV, ed. P Michel, F. E. DeMeo, & W. F. Bottke Tucson, AZ: Univ. Arizona Press), 375
Watanabe, S., Hirabayashi, M., Hirata, N., et al. 2019, Sci, 364, 268
Wilkison, S. L., Robinson, M. S., Thomas, P. C., et al. 2002, Icar, 155, 94
Wimarsson, J., Xiang, Z., Ferrari, F., et al. 2024, Icar, 421, 116223
Yu, Y., & Michel, P. 2018, Icar, 312, 128
Zacny, K., Bierhaus, E. B., Britt, D. T., et al. 2018, in Primitive Meteorites and Asteroids, ed. N. Abreu Amsterdam: Elsevier), 439
Zhang, Y., Michel, P., Barnouin, O. S., et al. 2022, NatCo, 13, 4589
Zhang, Y., Michel, P., Richardson, D. C., et al. 2021, Icar, 362, 114433
Zhang, Y., Richardson, D. C., Barnouin, O. S., et al. 2017, Icar, 294, 98